Femtosecond to millisecond structural changes in a light-driven sodium pump

Petr Skopintsev[1], David Ehrenberg[2,†], Tobias Weinert[1,†], Daniel James[1], Rajiv K. Kar[3], Philip J. M. Johnson[4], Dmitry Ozerov[5], Antonia Furrer[1], Isabelle Martiel[6], Florian Dworkowski[6], Karol Nass[6,7], Gregor Knopp[7], Claudio Cirelli[7], Christopher Arrell[8], Dardan Gashi[1,7], Sandra Mous[9], Maximilian Wranik[1], Thomas Gruhl[1], Demet Kekilli[1], Steffen Brünle[1], Xavier Deupi[1], Gebhard F. X. Schertler[1,10], Roger M. Benoit[1,11], Valerie Panneels[1], Przemyslaw Nogly[9], Igor Schapiro[3], Christopher Milne[7], Joachim Heberle[2], Jörg Standfuss[1]

[1]Laboratory of Biomolecular Research, Biology and Chemistry Division, Paul Scherrer Institut, 5232 Villigen, Switzerland.
[2]Experimental Molecular Biophysics, Department of Physics, Freie Universität Berlin, Berlin, Germany.
[3]Fritz Haber Center for Molecular Dynamics, Institute of Chemistry, The Hebrew University of Jerusalem, Jerusalem, Israel.
[4]Laboratory of Non-linear Optics, Photon Science Division, Paul Scherrer Institut, 5232 Villigen, Switzerland.
[5]Science IT, Paul Scherrer Institut, 5232 Villigen, Switzerland.
[6]Laboratory for Macromolecules and Bioimaging, Photon Science Division, Paul Scherrer Institut, 5232 Villigen, Switzerland.
[7]Laboratory of Femtochemistry, Photon Science Division, Paul Scherrer Institut, 5232 Villigen, Switzerland.
[8]Laboratory for Advanced Photonics, Photon Science Division, Paul Scherrer Institut, 5232 Villigen, Switzerland.
[9]Institute of Molecular Biology and Biophysics, Department of Biology, ETH Zürich, 8093 Zürich, Switzerland.
[10]Department of Biology, ETH Zurich, 8093 Zürich, Switzerland.
[11]Laboratory of Nanoscale Biology, Division of Biology and Chemistry, Paul Scherrer Institute, 5232 Villigen, Switzerland.

[†] These authors contributed equally

Summary

Light-driven sodium pumps actively transport small cations across cellular membranes[1]. They are used by microbes to convert light into membrane potential and have become useful optogenetic tools with applications in neuroscience. While resting state structures of the prototypical sodium pump *Krokinobacter eikastus* rhodopsin 2 (KR2) have been solved[2,3], it is unclear how structural alterations over time allow sodium translocation against a concentration gradient. Using the Swiss X-ray Free Electron Laser[4], we have collected serial crystallographic data at ten pump-probe delays from femtoseconds to milliseconds. High-resolution structural snapshots throughout the KR2 photocycle show how retinal isomerization is completed on the femtosecond timescale and changes the local structure of the binding pocket in the early nanoseconds. Subsequent rearrangements and deprotonation of the retinal Schiff base open an electrostatic gate in microseconds. Structural and spectroscopic data in combination with quantum chemical calculations indicate transient binding of a sodium ion close to the retinal within one millisecond. In the last structural intermediate at 20 ms after activation, we identified a potential second sodium binding site close to the extracellular exit. These results provide direct molecular insight into the dynamics of active cation transport across biological membranes.

This document is the accepted manuscript version of the following article:

Skopintsev, P., Ehrenberg, D., Weinert, T., James, D., Kar, R. K., Johnson, P. J. M., … Standfuss, J. (2020). Femtosecond-to-millisecond structural changes in a light-driven sodium pump. Nature. https://doi.org/10.1038/s41586-020-2307-8

Introduction

The preservation of sodium gradients across cellular membranes is critical to various biological functions. In living cells, the controlled flow of sodium is thus maintained by a series of specialized membrane channels and pumps. For example, glucose uptake in the guts and kidneys of mammals is fueled by a sodium gradient making glucose-sodium-symporters important pharmacological targets in the treatment of diabetes[5]. The opening and closing of voltage-gated sodium channels is responsible for the generation and propagation of neuronal signals. This has enabled the field of optogenetics, where light-sensitive microbial cation channels from the rhodopsin family are used as a key component for the manipulation of physiological responses in neurons or even living animals by light[6].

Rhodopsins are a functionally diverse family of proteins that rely on a retinal chromophore to harvest and sense light energy in microbes[7] and higher organisms[8]. In 2013, the family was extended by the discovery of light-driven sodium pumps from marine bacteria, where they maintain a low intracellular sodium ion concentration and generate membrane potential[1]. In optogenetic applications, the controlled light-induced outward pumping of sodium ions leads to neuronal inhibition under more physiological conditions compared to the use of related proton or chloride pumps[2]. The optogenetic application of the prototypical member of the class, *Krokinobacter eikastus* rhodopsin 2 (KR2), has been demonstrated with nematodes and with cortical rat neural cells[2]. Genetically engineered variants provide further possibilities to optimize KR2 for optogenetic applications[1-3,9-12].

The pumping cycle of KR2 has been studied by a variety of time-resolved spectroscopic techniques[1,13-19]. High-resolution structures of the resting state have been determined in various forms by X-ray crystallography[2,3,20]. However, in these studies the sodium substrate is not bound within the retinal binding pocket, indicating a substantially different pumping mechanism than in related ion pumps. Additional structural information on the reaction intermediates is required to understand how sodium can be actively transported out of the cell against substantial concentration gradients.

Time-resolved serial femtosecond crystallography (TR-SFX) allows the determination of structural snapshots of proteins that can be assembled into molecular movies of protein function. A series of classical targets have been characterized using the method including myoglobin[21], photoactive yellow protein[22,23] and bacteriorhodopsin (bR)[24-27]. In our present work, we used the Swiss X-ray Free Electron Laser (SwissFEL) to study structural changes in the more recently discovered sodium pump KR2 within a wide temporal window from 800 fs to 20 ms. Ten structural snapshots positioned at temporal delays coinciding with the

77 accumulation of intermediates identified by time-resolved absorption spectroscopy on
78 crystals show how the energy captured by the retinal leads to structural rearrangements.
79 Structural, spectroscopic and quantum chemical data indicate sodium binding between N112
80 and D251 followed by release via a second binding site between E11, N106 and E160 on the
81 extracellular side. Our integrated work thus elucidates the structural changes associated with
82 sodium ions being actively transported across a biological membrane.
83
84 **Results and Discussion**
85 **Photocycle in KR2 crystals**
86 As benchmark for the study of KR2 activation in the crystalline environment, we employed
87 time-resolved absorption spectroscopy in the infrared (IR) and in the ultraviolet/visible
88 (UV/Vis) region. As under the original acidic crystallization conditions KR2 exhibits an
89 accelerated photocycle, we developed a soaking protocol to increase pH in the presence of
90 sodium ions (**Extended Data Fig. 1**). The treatment changes the color of crystals from blue
91 to red with associated changes in the retinal binding pocket. Most importantly in terms of
92 function, KR2 in treated crystals follows a photocycle (**Fig. 1**) identical to that observed by
93 our absorption spectroscopy on purified KR2 in agreement with previous reports[19,18].
94 Sodium is expected to bind after deprotonation of the retinal Schiff base (SB) in the M
95 intermediate followed by release in the late O intermediate because the transition between
96 these spectroscopic intermediates is dependent on sodium concentration[28]. At acidic pH,
97 characteristic O-related bands are absent (**Extended Data Fig. 2**), while at higher pH in the
98 presence of sodium these bands reach maximal amplitude a few milliseconds after activation.
99 A dependency on sodium concentration is evident in the TR-IR data through changes in both
100 amplitude and kinetics of the M-O transition (**Fig. 1, d**). Clearly, KR2 in treated crystals
101 responds to the presence of sodium with a kinetic profile compatible with light-driven sodium
102 pumping. Accordingly, all crystals for the dynamic measurements described below were
103 rebuffered in the presence of sodium before injection across the X-ray laser pulses.
104
105 **Structural changes over time**
106 In three days of beamtime during the first user run of SwissFEL, we collected 158'832 dark
107 (pump laser off) and 496'904 light (pump laser on) indexable diffraction patterns with an
108 anisotropic resolution up to 1.6 Å (**Extended Data Tab. 1, Extended Data Fig. 3, a**). The
109 light data were distributed over ten time delays (Δt= 800 fs, 2 ps, 100 ps, 1 ns, 16 ns, 1 μs, 30

110 μs, 150 μs, 1 ms and 20 ms) between the optical pump and the X-ray probe pulses (**Extended**
111 **Data Fig. 4, a**). These time delays were selected based on our TR-IR data and on previous
112 ultrafast stimulated Raman spectroscopic experiments[16], to cover critical steps in the KR2
113 photocycle. The serial crystallographic structure of the KR2 resting state closely resembles
114 structures solved by conventional cryo-crystallography (**Extended Data Fig. 5**). Progressing
115 from this starting point, isomorphous difference electron density maps (F_o(light)-F_o(dark))
116 allow to follow structural changes over time. Extrapolated data were used to refine molecular
117 structures for each individual time delay. The light-activated structures follow a continuous
118 evolution of structural rearrangements that we combined into five different stages
119 (800fs+2ps, 1ns+16ns, 30μs+150μs, 1ms and 20ms) based on root-mean-square deviations
120 between the models (**Extended Data Fig. 4, b**). These five structural intermediates provide
121 direct molecular insights into the sequence of structural rearrangements during the KR2
122 pumping cycle.
123
124 **Retinal and transmission of light energy**
125 The first stage in the structural evolution of KR2 activation ranges from femto- to
126 picoseconds with structural rearrangements centered at the retinal chromophore, the principal
127 photochemical switch of all rhodopsins. Retinal is covalently bound via a protonated SB
128 linkage to K255 in helix G in the core of KR2. Similar to other microbial rhodopsins,
129 absorption of a photon in KR2 leads to retinal isomerization at the C13=C14 bond (**Extended**
130 **Data Fig. 3, b**). This photochemical process is faster than in the related proton pump bR,
131 with formation of the earliest photointermediate already after about 200 fs[16], which is
132 consistent with a fully isomerized 13-*cis* retinal in our earliest difference electron density at
133 Δt= 800 fs and after structural refinement at Δt= 800fs+2ps (**Fig. 2, a**). Within the early time
134 delays, we further observed a shift of w406 and the retinal counterion D116, similar, but less
135 pronounced compared to the ultrafast adaptation of bR[25]. A clear difference to bR is that the
136 isomerized retinal is pointing in the opposite direction in KR2 with the C20 methyl group
137 tilting towards helix C instead of helix G. The direction could already be pre-determined in
138 the resting state as, compared to bR, the retinal polyene KR2 is bend in the opposite
139 direction.
140 The second distinct stage within the structural evolution takes place in the nanosecond range
141 (**Fig. 2, b**), when early conformational changes of the protein backbone occur. In bR,
142 adaptation of the energetically more favorable planar 13-*cis* conformation pushes the

143 straightening retinal "upwards" against W182 in helix F to displace it towards the
144 cytoplasmic side[24]. In KR2, the changes involving the structurally equivalent W215 are
145 absent, instead, the retinal C20 methyl group pushes "sideways" in the membrane plane
146 against V117. Starting at Δt= 1 μs and rising until the later microsecond delay, the difference
147 density maps indicate a flip of V117 and an established transmission of structural changes
148 into helix C (**Fig. 2, c**). In this way, the light energy stored in the early photoproducts
149 propagates into the seven-transmembrane helical bundle to fuel larger conformational
150 changes at later times.
151
152 **Sodium translocation and gating**
153 The third and fourth stages of the structural evolution from microseconds to milliseconds
154 correlate with the temporal range relevant for sodium translocation[19,28]. Starting from Δt= 1
155 μs, clear electron difference density peaks above 3.5 σ show how Y218 in helix F and S254
156 in helix G approach the position of retinal in the resting state. Changes are further transmitted
157 several turns along helix G towards the intracellular side. Structural refinement resulted into
158 small shifts of helix C in the order of 1 Å in the Δt= 30μs+150μs structural intermediate and
159 additional changes along helix D occur in the two millisecond delays. These rearrangements
160 (**Fig. 3**) are of particular interest because they are close to the putative entry and exit routes
161 for sodium[2,3].
162 One half of the translocation pathway connects the retinal binding pocket between helices C,
163 F and G with a water-filled cavity on the intracellular side. It passes N61 and G263 at the
164 entry side and Q123 of the NQD motif, three residues important for ion selectivity[3,11,13].
165 Native KR2 pumps lithium and sodium ions, yet not larger cations like potassium[1]. In their
166 hydrated forms the size of sodium is larger than that of potassium, but the dehydrated sodium
167 ion is smaller than potassium[29,31]. This suggests that the selective pumping of sodium ions
168 must involve dehydration, which likely happens at the entry of the conducting pathway[31].
169 The narrowest part of the sodium translocation pathway in the light-activated structures of
170 KR2 passes between the retinal and the side chains of D116 and K255, acting as a counterion
171 and covalent link for the retinal, respectively. Neutralization of the retinal SB through proton
172 transfer and transient widening at this position likely acts as an electrostatic gate (**Fig. 4, a,**
173 **Extended Data Vid. 1**) that allows the selective passage of cations[2,3,32]. The distance
174 between the retinal SB and D116 contracts by about 0.5 Å at Δt= 1ns+16ns, which favors
175 proton transfer in the transition to the M intermediate[33]. At Δt= 30μs+150μs the distance

176 widens again in agreement with the spectroscopic data indicating deprotonation of the SB and
177 occurrence of the M state in the early microseconds (**Fig. 1**). With 1.4 Å, the opening seems
178 small for a 1.9 Å sodium ion to pass. At this point we cannot exclude that the gate does not
179 fully open in our crystals formed from monomeric KR2, since pentameric KR2 can adopt a
180 more open conformation in the SB region[3,20] and mutations in the oligomerization interface
181 can affect pumping efficiency[1,17,20] (for further discussion see **Extended Data Fig. 5**).
182 However, stable structural intermediates that accumulate in time-resolved studies of molecule
183 ensembles do not necessarily reveal all functional steps[34] and our integrated structural,
184 spectroscopic and computational analysis is compatible with sodium binding in the later
185 stages (see below). Most probably, approach of a sodium ion and electrostatic weakening of
186 the helix C-SB interaction allows formation of a transient pathway within the L/M
187 equilibrium in the microseconds.
188 The fifth stage in the late milliseconds is related to changes in the section of the translocation
189 pathway extending from the retinal binding site towards the extracellular side of the protein.
190 Here the bottlenecks run along the side chain of R109 in agreement with mutations at this
191 positions transforming KR2 into a light-gated inward facing potassium channel[35]. A rotamer
192 change of R109 and Q78 together with a shift of helix D at Δt= 20 ms indicates an opening
193 which connects the water-filled cavity in vicinity of the retinal with a second water-filled
194 cavity close to E11, N106, E160 and R243 towards the exit site on the extracellular side of
195 the membrane.
196
197 **Formation of sodium binding sites**
198 In the alternate access model of active membrane transport, the substrate is bound while the
199 protein rearranges to allow release without backflow. Light-driven sodium pumps like KR2
200 do not bind substrate close to the retinal SB in the resting state[1-3]. Hence, the question
201 remains where the transported sodium ion is located and how it moves across the membrane
202 with time. Time-resolved IR spectroscopy on a protein film (this work and[19]) and crystals
203 provides evidence (through a marker band at 1688 cm^{-1}) of changes in the environment of an
204 asparagine residue peaking in the O intermediate within milliseconds under sodium pumping
205 conditions (**Fig. 1, Extended Data Fig. 2**). Mutagenesis of N112 and D251 close to the
206 retinal binding pocket abolish sodium pumping[13,35,36] and the two residues have been
207 suggested as potential sodium coordination partners based on molecular dynamic
208 simulations[32] and structural comparisons to other rhodopsins[37] (**Extended Data Fig. 6**).

209 Analysis of our TR-SFX data shows an interesting evolution of the electron density in this
210 region (**Fig. 3 c, d**). At Δt= 1 ms a clear positive difference peak is located about 1 Å away
211 from w406 in the resting state and close to N112 and D251. The electron densities of water
212 and sodium ions have an identical signature in X-ray crystallographic data, yet the
213 environment can provide clues to the nature of the detected atoms[38]. At Δt= 1ms the density
214 peak is shifted away from the amine group of W113 and positively charged R109, both
215 coordinating w406 in the resting state but unable to bind sodium. The new position is with
216 2.5 Å towards N112 and D251, which is close to the ideal coordination distance for a sodium
217 ion[39] concurring with our spectroscopic data. We validated the position of the putative
218 sodium ion using hybrid quantum mechanics/molecular mechanics (QM/MM) calculations.
219 Inclusion of the sodium in the Δt= 1 ms structure resulted in a large spectral red shift of 55
220 nm with respect to the electronic absorption band of the resting state, while placing water at
221 this position yields a 11 nm blue shift (**Fig. 4, b, c,**). The experimental value obtained from
222 the transient spectroscopic data is a red shift of 66 nm and hence inclusion of the sodium ion
223 is necessary to reproduce the absorption maximum of the O intermediate (λ_{max}= 592 nm).
224 The absorption shift is not a direct effect but due to changes in the D116-SB interaction
225 through N112. It is reasonable to suggest that through alteration of this H-bonding network
226 sodium binding favors SB reprotonation, and with this blocks the backflow of ions.
227 At Δt= 20 ms, the electron density close to the retinal binding pocket fades below the 3 σ
228 level indicating release of the sodium ion. Further along the translocation pathway we
229 observe the formation of a second sodium binding site close to the extracellular side of the
230 membrane. Here, a clear positive difference peak appears between E11, N106 and E160. In
231 the same temporal regime, the shift of R243 moves a positive charge away to facilitate
232 sodium binding (**Fig. 3 e, f**). Again, the coordination distances of 2.4 Å to N106 and 2.5 Å to
233 E11 support our assignment of a sodium ion in this putative binding site. Of particular note is
234 the observation that both sodium binding sites employ displacements of arginine residues to
235 favor sodium binding over water. The corresponding positions of these residues have
236 functional equivalents in bR (**Extended Data Fig. 6**) with R109 close to the retinal binding
237 pocket corresponding to R82 critical for proton transfer in bR. The position of R243 in KR2
238 is occupied by E194 in bR, which is part of the proton release group. Some key sites in the
239 seven-transmembrane helical bundle seem to be functionally conserved throughout evolution
240 but are approached at different times within their respective pumping cycles.
241

Conclusions

Our data allow to assemble a molecular movie of structural changes in KR2 and to propose a basic mechanistic model of light-driven sodium transport (**Video 1**). The unidirectional flow of ions is achieved by minimal structural changes that generate ion selectivity and prevent ion back leakage into the cell. Our observation of active ion pumping is consistent with general concepts of ion pumping across a biological membrane by the alternate access model, illustrating them with high-resolution structures of the intermediate steps. It will be an interesting topic for future studies how pH and long-range cooperative effects between protomers influence these structural dynamics. X-ray lasers now provide the means to study how single point mutations allow translocation of larger ions like potassium[3] and cesium[11] or turn KR2 from an active pump into a passive channel[35]. Deeper insights into the transport mechanisms found in microbial rhodopsins will demonstrate how nature adapted a common leitmotif to different functions and facilitate the design of variants for neurobiological applications in optogenetics.

Acknowledgements

This project was founded by the following agencies: The Swiss National Science Foundation project grants 31003A_141235 and 31003A_159558 (to J.S.), PZ00P3_174169 (to P.N.) and 310030B_173335 (to G.S.). We further acknowledge support by the NCCR:MUST (to C.M. and J.S.). The German Research Foundation supported the work through SFB-1078, project B3 and SPP-1926, HE 2063/6-1 (to J.H). This project has received funding from the European Union's Horizon 2020 research and innovation program under the Marie-Sklodowska-Curie grant agreement No 701646 and 701647. I.S. gratefully acknowledges funding by the European Research Council (ERC) under the European Union's Horizon 2020 research and innovation program (Grant No. 678169 ''PhotoMutant''). I.S. thanks the SFB 1078 ''Protonation Dynamics in Protein Function'' for the Mercator fellowship. R.K.K. acknowledges support from the Lady Davis Trust for the Arskin postdoctoral fellowship. We would like to acknowledge the fruitful discussions with Dr. Niranjan Varma on TR-SFX sample jetting. We are grateful for excellent support from the Macromolecular Crystallography group during testing of crystals at the Swiss Light Source.

Author contributions

The project was initiated and coordinated by J.S. following input on crystallographic data evaluation from T.W., quantum chemical calculations from I.S., pump-probe experiments at

the ALVRA endstation from C.M. and time-resolved spectroscopy from J.H.. The KR2 expression construct was cloned by R.M.B.. The protein was expressed, prepared and crystallized by P.S. with help from A.F.. A constant supply of sample during the beamtime was secured with the help of A.F., T.G., M.W., D.E., D.K. and R.M.B. using protocols developed by P.S.. Crystal injection was optimized by P.S. and D.J.. The lipidic cubic phase injector was operated and aligned during the beamtime by D.J., F.D., I.M. and D.G.. The endstation including the laser system were aligned and operated by P.S., K.N., G.K., C.C. and C.M who also designed the Alvra prime pump-probe station. C.A. and P.J.M.J. operated the timing diagnostics during the experiment. The SFX data analysis pipeline was built and operated by D.O. and K.N. Data processing during the beamtime was done by T.W., P.N. and S.B.. S.M., V.P. and X.D. recorded progress during data collection and/or in a previous test beamtime. Final structures were refined by P.S. and T.W. and interpreted together with J.S.. Quantum chemical calculations were done by R.K.K. and I.S.. The time-resolved spectroscopic experiments were done by D.E. and P.S. and interpreted together with J.H.. The manuscript was written by J.S. with direct contributions from P.S., T.W., D.E., J.H., R.K.K., I.S. and further suggestions from most of the other authors. All authors read and acknowledged the manuscript.

Author Information

Reprints and permissions information is available at www.nature.com/reprints. Correspondence and requests for materials should be addressed to joerg.standfuss@psi.ch.

Competing interests

The authors declare to have no competing interests.

Data availability

Resting state coordinates and structure factors have been deposited in the PDB database under accession code 6TK7 (acidic pH) and 6TK6 (neutral pH). Together with the neutral pH resting state structure the light activated data for all time points (800 fs, 2 ps, 100 ps, 1 ns, 16 ns, 1µs, 30 µs, 150 µs, 1ms and 20 ms) was deposited in the mmCIF file. For the refined structures using combined data (800fs+2ps, 1ns+16ns and 30µs+150µs) and single (1ms and 20ms) light activated data sets, coordinates, light amplitudes, dark amplitudes and extrapolated structure factors have been deposited in the PDB database under accession codes 6TK5 (800fs+2ps), 6TK4 (1ns+16ns), 6TK3 (30µs+150µs), 6TK2 (1 ms) and 6TK1 (20 ms).

Fig. 1: Time-resolved absorption measurements on KR2 in solution and crystals. Spectra from (**a**) purified KR2 and (**b**) in the crystalline phase prepared in analogy to the TR-SFX experiment. The upper panel depicts experiments in the infrared covering the C=C stretch mode of the retinal up to amide I vibrations originating from the protein backbone. The middle panel presents changes in the UV/Vis region on the same sample. A global fit analysis of the infrared data shown in the bottom panel revealed the presence of intermediate states K_L, L/M, O_1 and O_2. (**c**) Model of the photocycle of KR2 derived from time-resolved absorption spectroscopy. (**d**) Sodium-dependency of the 1516 cm^{-1} marker band for the O intermediate in KR2 crystals under TR-SFX conditions. Time traces were normalized to the ground state bleach signal and fitted by the sum of three connected exponentials.

Fig. 2: Early steps in the activation of a light-driven sodium pump. Difference electron density maps (F_o(light) - F_o(dark), negative density in gold and positive density in blue shown at 3.5 σ) and structural refinements (resting state shown in grey and light activated in color) show the early rearrangements at (**a**) Δt= 800fs + 2ps, (**b**) Δt= 1ns + 16ns, (**c**) Δt= 30µs + 150µs. Superposition of structures illustrates how retinal isomerization translates the light energy into structural changes (**d**) via V117 in helix C in case of KR2 (resting state shown as grey sticks, the structures at Δt= 2ps shown as blue sticks and Δt= 1 µs shown as green sticks) and (**e**) via W182 in helix F in case of bR (data and coordinates taken from[24,25], resting state shown as grey sticks, the structures at Δt= 10ps shown as blue sticks and Δt= 0.8 µs shown as green sticks). Arrows indicate structural changes discussed in the main text.

Fig. 3: Structural changes along the sodium translocation pathway. (**a**) Overview of the KR2 structure with the suggested route of sodium translocation across the membrane identified using the program Caver[40] (blue and red surfaces for the two halves plotted on the structure at Δt= 1 ms with changes in color indicating functionally critical regions). Selected residues and the retinal chromophore are shown as sticks. (**b**) Structural refinements and comparison to the resting state show how the protein rearranges from nanoseconds to milliseconds (blue to red gradient and ribbon width indicate rmsd to the resting state). Close-up view into the region of the retinal SB (**insets c, d**) and the extracellular side of the membrane (**insets e, f**). The structural rearrangements are compatible with the formation of a transient sodium binding site between N112 and D251 at Δt= 1 ms (**c**) and a second site further along the translocation pathway between E11, N106 and E160 at Δt= 20 ms after photoactivation (**f**). Difference electron density maps (F_o(light) - F_o(dark)) shown with negative density in gold and positive density in blue countered at 3.2 σ) and arrows highlight structural changes discussed in the main text.

Fig. 4: Electrostatic gating mechanism. (**a**) Circles show the retinal binding pocket at critical steps in the KR2 photocycle. The positive charge of the retinal SB is shown in blue and the negative charge at the D116 counterion is shown in red. Arrows indicate steps in sodium translocation including light-induced retinal isomerization and conformational rearrangements in the retinal binding pocket, entry of a sodium ion after proton transfer from the SB to the counterion, binding of the sodium ion and reprotonation of the retinal SB and ion release. QM/MM optimized geometry with water (**b**) or sodium ion (**c**) in the binding site between N112 and D251. The spectral shift is only in line with the spectroscopic data on the redshifted O intermediate (**Compare Fig. 1 and Extended Data Fig. 6, h**) when sodium is included. The shift is not a direct effect but is due to the change in the D116-SB interaction through N112 via the shown hydrogen-bonding network (dashed lines). For a dynamic illustration of the described rearrangements compare **Video 1**.

References

1. Inoue, K. *et al.* A light-driven sodium ion pump in marine bacteria. *Nature Communications* **4,** (2013).
2. Kato, H. E. *et al.* Structural basis for Na+ transport mechanism by a light-driven Na+ pump. *Nature* **521,** 48–U347 (2015).
3. Gushchin, I. *et al.* Crystal structure of a light-driven sodium pump. *Nat. Struct. Mol. Biol.* **22,** 390–U61 (2015).
4. Milne, C. *et al.* SwissFEL: The Swiss X-ray Free Electron Laser. *Applied Sciences* **7,** 720 (2017).
5. Poulsen, S. B., Fenton, R. A. & Rieg, T. Sodium-glucose cotransport. *Curr. Opin. Nephrol. Hypertens.* **24,** 463–469 (2015).
6. Deisseroth, K. Optogenetics: 10 years of microbial opsins in neuroscience. *Nat. Neurosci.* **18,** 1213–1225 (2015).
7. Govorunova, E. G., Sineshchekov, O. A., Li, H. & Spudich, J. L. Microbial Rhodopsins: Diversity, Mechanisms, and Optogenetic Applications. *Annual review of Biochemistry* **86,** 845–872 (2017).
8. Terakita, A. The opsins. *Genome Biol.* **6,** 213 (2005).
9. Grimm, C., Silapetere, A., Vogt, A., Bernal Sierra, Y. A. & Hegemann, P. Electrical properties, substrate specificity and optogenetic potential of the engineered light-driven sodium pump eKR2. *Sci Rep* **8,** 9316 (2018).
10. Hoque, M. R. *et al.* A Chimera Na+-Pump Rhodopsin as an Effective Optogenetic Silencer. *PLoS ONE* **11,** e0166820 (2016).
11. Konno, M. *et al.* Mutant of a Light-Driven Sodium Ion Pump Can Transport Cesium Ions. *J Phys Chem Lett* **7,** 51–55 (2016).
12. Inoue, K. *et al.* Red-shifting mutation of light-driven sodium-pump rhodopsin. *Nature Communications* **10,** 1993 (2019).
13. Inoue, K., Konno, M., Abe-Yoshizumi, R. & Kandori, H. The Role of the NDQ Motif in Sodium-Pumping Rhodopsins. *Angew. Chem. Int. Ed. Engl.* **54,** 11536–11539 (2015).
14. Tahara, S. *et al.* Ultrafast photoreaction dynamics of a light-driven sodium-ion-pumping retinal protein from Krokinobacter eikastus revealed by femtosecond time-resolved absorption spectroscopy. *J Phys Chem Lett* **6,** 4481–4486 (2015).
15. Tahara, S. *et al.* Origin of the Reactive and Nonreactive Excited States in the Primary Reaction of Rhodopsins: pH Dependence of Femtosecond Absorption of Light-Driven Sodium Ion Pump Rhodopsin KR2. *J Phys Chem B* **122,** 4784–4792 (2018).

16. Hontani, Y. *et al.* The photochemistry of sodium ion pump rhodopsin observed by watermarked femto- to submillisecond stimulated Raman spectroscopy. *Phys Chem Chem Phys* **18,** 24729–24736 (2016).
17. Kaur, J. *et al.* Solid-state NMR analysis of the sodium pump Krokinobacter rhodopsin 2 and its H30A mutant. *J. Struct. Biol.* (2018). doi:10.1016/j.jsb.2018.06.001
18. Chen, H.-F. *et al.* Time-resolved FTIR study of light-driven sodium pump rhodopsins. *Phys Chem Chem Phys* **20,** 17694–17704 (2018).
19. Asido, M. *et al.* Time-resolved IR spectroscopy reveals mechanistic details of ion transport in the sodium pump Krokinobacter eikastus rhodopsin 2. *Phys Chem Chem Phys* **21,** 4461–4471 (2019).
20. Kovalev, K. *et al.* Structure and mechanisms of sodium-pumping KR2 rhodopsin. *Science Advances* **5,** eaav2671 (2019).
21. Barends, T. R. M. *et al.* Direct observation of ultrafast collective motions in CO myoglobin upon ligand dissociation. *Science* **350,** 445–450 (2015).
22. Tenboer, J. *et al.* Time-resolved serial crystallography captures high-resolution intermediates of photoactive yellow protein. *Science* **346,** 1242–1246 (2014).
23. Pande, K. *et al.* Femtosecond structural dynamics drives the trans/cis isomerization in photoactive yellow protein. *Science* **352,** 725–729 (2016).
24. Nango, E. *et al.* A three-dimensional movie of structural changes in bacteriorhodopsin. *Science* **354,** 1552–1557 (2016).
25. Nogly, P. *et al.* Retinal isomerization in bacteriorhodopsin captured by a femtosecond X-ray laser. *Science* **aat0094,** 10.1126–science.aat0094 (2018)
26. Weinert, T. *et al.* Proton uptake mechanism in bacteriorhodopsin captured by serial synchrotron crystallography. *Science* **365,** 61–65 (2019).
27. Nass Kovacs, G. *et al.* Three-dimensional view of ultrafast dynamics in photoexcited bacteriorhodopsin. *Nature Communications* **10,** 3177 (2019).
28. Kato, Y., Inoue, K. & Kandori, H. Kinetic Analysis of H+-Na+ Selectivity in a Light-Driven Na+-Pumping Rhodopsin. *J Phys Chem Lett* **6,** 5111–5115 (2015).
29. SHANNON, R. D. Revised Effective Ionic-Radii and Systematic Studies of Interatomic Distances in Halides and Chalcogenides. *Acta Crystallographica Section A* **32,** 751–767 (1976).
31. Kandori, H., Inoue, K. & Tsunoda, S. P. Light-Driven Sodium-Pumping Rhodopsin: A New Concept of Active Transport. *Chem. Rev.* **118,** 10646–10658 (2018).
32. Suomivuori, C.-M., Gamiz-Hernandez, A. P., Sundholm, D. & Kaila, V. R. I. Energetics and dynamics of a light-driven sodium-pumping rhodopsin. *Proc. Natl. Acad. Sci. U.S.A.* **114,** 7043–7048 (2017).
33. Nishimura, N., Mizuno, M., Kandori, H. & Mizutani, Y. Distortion and a Strong Hydrogen Bond in the Retinal Chromophore Enable Sodium-Ion Transport by the Sodium-Ion Pump KR2. *J Phys Chem B* **123,** 3430–3440 (2019).
34. Ourmazd, A. Cryo-EM, XFELs and the structure conundrum in structural biology. *Nat. Methods* **16,** 941–944 (2019).
35. Vogt, A. *et al.* Engineered Passive Potassium Conductance in the KR2 Sodium Pump. *Biophys. J.* **116,** 1941–1951 (2019).
36. Abe-Yoshizumi, R., Inoue, K., Kato, H. E., Nureki, O. & Kandori, H. Role of Asn112 in a Light-Driven Sodium Ion-Pumping Rhodopsin. *Biochemistry* **55,** 5790–5797 (2016).
37. Gushchin, I. *et al.* Structure of the light-driven sodium pump KR2 and its implications for optogenetics. *FEBS J.* **283,** 1232–1238 (2016).
38. Zheng, H. *et al.* CheckMyMetal: a macromolecular metal-binding validation tool. *Acta Crystallogr D Struct Biol* **73,** 223–233 (2017).

463 39. Zheng, H., Chruszcz, M., Lasota, P., Lebioda, L. & Minor, W. Data mining of metal
464 ion environments present in protein structures. *J. Inorg. Biochem.* **102,** 1765–1776
465 (2008).
466 40. Chovancova, E. *et al.* CAVER 3.0: a tool for the analysis of transport pathways in
467 dynamic protein structures. *PLoS Comput. Biol.* **8,** e1002708 (2012).
468

469 **Methods**
470

471 **Cloning, protein expression and purification**

472 The KR2 construct with a TEV-cleavable C-terminal 6xHis-tag was cloned into the
473 pStaby1.2 vector (Delphi Genetics, Belgium). Protein expression was performed in
474 C41(DE3) E. *coli* cells. The cells grew in shaking smooth flasks with Luria Broth at 37 °C.
475 Expression was induced by addition of 1 mM β-D-thiogalactopyranoside (IPTG) at an
476 OD600 of ~0.8. Following overnight expression at 37 °C in the presence of 10 μM all-*trans*
477 retinal, the bacterial cultures were harvested by centrifugation at 5,000 g for 15 minutes. The
478 cell pellets were disrupted with Avestin EmulsiFlex-C3 homogenizer at 15,000 psi in lysis
479 buffer (20 mM Tris pH 8.0, 5% glycerol, 0.5% Triton X-100, 5 μg/ml DNase I and
480 cOmpleteTM protease inhibitor tablets, Roche), and the membrane fraction was collected
481 with ultracentrifugation at 90,000 g. The membrane pellet was resuspended with IKA T 25
482 Ultra-Turrax disperser in solubilization buffer that contained 50 mM Tris pH 8.0, 300 mM
483 NaCl, cOmplete^{TM} protease inhibitors, 1.0% n-Dodecyl β-D-maltoside (DDM, Anatrace),
484 0.2% cholesteryl hemisuccinate (CHS, Anatrace), and stirred overnight at 4 °C. The
485 overnight suspension was subjected to a second round of ultracentrifugation before the
486 supernatant was applied to Immobilized Metal Affinity Chromatography (IMAC), and further
487 washed with IMAC buffer (50 mM Tris pH 8.0, 150 mM NaCl, 100 mM Imidazole, 0.02%
488 DDM, 0.04% CHS). The bound protein was eluted by addition of 500 mM imidazole in
489 IMAC buffer. TEV protease was added, and the KR2-TEV cleavage solution was sealed in
490 an 8 kDa M_w cutoff dialysis membrane and dialyzed against 50 mM Tris pH 8.0, 150 mM
491 NaCl, 0.02% DDM, 0.04% CHS buffer overnight. The TEV-cleaved solution was re-applied
492 to the IMAC column, and the flow-through was collected and concentrated with a centrifugal
493 filter device (Millipore 100 kDa M_w cutoff). The concentrated protein sample was loaded
494 onto a HiLoad Superdex 75 prep grade 16/600 column (GE Healthcare) equilibrated with
495 SEC buffer (50 mM Tris pH 8.0, 150 mM NaCl, 0.05% DDM, 0.01% CHS). The elution
496 profile was monitored at 280 nm and 530 nm with Shimadzu UV-2401PC spectrophotometer
497 (Kyoto, Japan), and the purest fractions were concentrated to ~100 mg/ml, flash frozen in
498 liquid nitrogen and stored at -80 °C until further crystallization.

499

500 **Crystallization and TR-SFX sample preparation**

501 Crystallization was carried out in lipidic cubic phase (LCP) using conditions similarly as
502 described in ref[2]. The purified protein buffer and monoolein (1-Oleoyl-rac-glycerol, Nu-Chek
503 prep) were thoroughly mixed in a 2:3½ v/v ratio through coupled gas-tight Hamilton
504 syringes. The formed LCP was extruded through Hamilton needles into plastic B-Braun
505 Omnifix®-F syringes loaded with precipitant (200 mM Sodium Acetate pH 4.4, 150 mM
506 $MgCl_2$, 35% PEG 200). Crystallization occurred overnight in the dark at 20 °C and yielded
507 plate-like blue KR2 crystals with dimensions of 10-30×10-25×1-3 μm^3 (**for a size**
508 **distribution see Extended Data Fig. 1, c**).

509 Following formation of crystals, the precipitant solution was washed out by soaking the LCP
510 in excess 150 mM NaCl, 35% PEG 200 solution, two times for 48 hours in total. The washed
511 phase with unbuffered crystals having blue color was further harvested into gastight
512 Hamilton syringes in 60 µl fractions, and doped with 33 µl monoolein and 3.0 µl 50% PEG
513 1500 to form a stable jetting phase. Prior to data collection, the phase with crystals was
514 mixed with LCP prepared from monoolein and 1 M Tris pH 9.0, 150 mM NaCl, 35% PEG
515 200 through a three-way syringe coupler[41]. The volumes of the mixed phases were picked
516 such that the water fraction of the mesophase would contain 200 mM Tris, 150 mM NaCl,
517 35% PEG 200 and PEG 1500 and the blue KR2 crystals changed color to red upon mixing
518 (**Extended Data Fig. 1**). While the mixing was done with Tris solution at pH 9.0, the final
519 pH of the preparation was close to pH 8 as confirmed by litmus paper. We attribute this shift
520 by one pH unit and the shift in color transition as compared to KR2 solution to possible
521 residual buffer trapped in LCP and/or buffering capacity of monoolein molecules. Jetting
522 stability of the mixed phase was confirmed before the XFEL experiment with a high-speed
523 camera setup described in[41] (**Video 2**).

524

525 **Experimental setup and XFEL data collection**

526 The TR-SFX data on KR2 crystals were collected in February 2019 in three days at the Alvra
527 experimental station of SwissFEL. X-ray pulses with a photon energy of 12 keV and a pulse
528 energy of 400 µJ at a repetition rate of 50 Hz were used for the experiment. On average 180
529 µJ (9×10^{10} X-ray photons) per pulse were deposited onto a 2.6 × 3.6 μm^2 spot (FWHM),
530 focused by Kirkpatrick-Baez mirrors. The X-ray intensity was adjusted using solid
531 attenuators to maximize diffraction signal without disrupting the sample injector flow or
532 damaging the detector. To reduce X-rays scattering, the air in the sample chamber was

533 pumped down to 100-200 mbar while being substituted with helium. To reduce the amount of
534 data the Jungfrau 16M detector was run in 4M mode excluding the outer panels.
535 KR2 crystals were loaded into a high viscosity injector connected to an HPLC pump[54]. The
536 crystals were extruded into the pump-probe interaction point through a 75 μm capillary at a
537 flow rate of 3.35 μl per minute. In the interaction point, the probe XFEL beam intersected
538 with a circularly polarized pump beam originating from an optical parametric amplifier
539 producing laser pulses with 150 fs duration ($1/e^2$), 575 nm wavelength and 3 μJ total energy
540 in a focal spot of 80 × 80 μm^2 beam ($1/e^2$), corresponding to a maximal laser fluence of 59
541 mJ/cm^2 and laser power density of 397 GW/cm^2. Approximating the dose per KR2 molecule
542 with the Lambert-Beer law for an average 19 × 16 × 2 μm^3 sized crystal, we estimated that
543 8.3-3.5 photons per retinal are absorbed, depending on the crystal's orientation and the
544 position of the individual chromophore within the optically dense crystal. However, the
545 average photon dose is certainly lower because scattering and reflection on the extruded
546 material further reduces the doses with estimates ranging from 20%[27] to 90%[55]. Our previous
547 best estimate was 80% for TR-SFX experiments on bR[25], which would reduce the calculated
548 doses to 1.7-0.7 photons per retinal. Another point to consider is that the Sn ← S1 excited-
549 state absorption is in the 400–500 nm region[15]. As such the excited state is unlikely to absorb
550 a 575 nm photon further minimizing the chance of multi-photon absorption.
551 To cover the KR2 photocycle time delays between the pump laser and the probing XFEL
552 pulses were chosen at Δt = 800 fs, 2 ps, 100 ps, 1 ns, 16 ns, 1 μs, 30 μs, 150 μs, 1 ms. An
553 additional time delay at 20 ms was created by shifting the laser focus position and using the
554 50 Hz XFEL repetition rate to create a delay to the pump laser.
555 Every fifth pulse of the pump laser was blocked, so that a series of four light-activated and
556 one dark diffraction pattern were collected in sequence. Roughly 50,000 light-activated
557 patterns were collected for each time delay, a high-quality dark dataset was obtained by
558 merging patterns of the fifth pulse, and ~50,000 patterns with pump laser off. These laser off
559 images were also acquired for comparison, to confirm that the dark data in each cycle was not
560 illuminated. Finally, about 40,000 patterns were obtained with no laser activation for
561 untreated crystals at acidic pH, to compare with crystals soaked as described above. For
562 clarity, the applied data collection scheme is illustrated in **Extended Data Fig. 4**.
563
564 **Data processing**
565 All data were indexed, integrated and merged using Crystfel[56,57] version 0.8.0. Data were
566 indexed using the xgandalf[58] and taketwo[59] algorithms. Data were integrated using the --rings

567 option in indexamajig. Patterns were merged using partialator with the following options: --
568 model=unity, --iterations=3. No per-pattern resolution cutoff was applied. Data showed
569 diffraction anisotropy of about 2.2 x 2.2 x 1.6 Å along a*, b* and c*. The general resolution
570 cutoff of 1.6 Å has been chosen after evaluating all uncut datasets using the staraniso
571 server[48], showing a maximal resolution of 1.6 Å for most datasets (**Extended Data Table 1**).
572 Diffraction intensities of each individual dataset output from partialator where cut at 1.6 Å
573 resolution and subjected to the staraniso server again. The staraniso server determines the
574 resolution cutoff for each dataset based on the signal-to-noise ratio in a given resolution shell
575 and then truncates data along these directions, in case of KR2 this resulted in data truncation
576 very close to the given ellipsoid dimensions. It is currently not possible to generate a merged
577 dataset from serial crystallographic data using staraniso, therefore we generated datasets
578 containing only reflections that were kept by staraniso and generated statistics from them
579 using CrystFEL. Refinements for dark data collected at acidic and neutral pH were carried
580 out to the full resolution range against data obtained after anisotropic truncation. Since data
581 extrapolation lowers the data quality, we lowered the resolution cutoff for structural
582 refinements of the combined data (800fs+2ps, 1ns+16ns and 30µs+150µs) to 2.25 Å
583 resolution and of the smaller datasets at 1 ms and 20 ms to 2.5 Å. The truncated datasets were
584 deposited to the world wide Protein Data Bank (wwwPDB)[60] together with the structures
585 (**Extended Data Table 2**) refined against original (resting acidic pH and resting neutral pH)
586 and extrapolated data (800fs+2ps, 1ns+16ns, 30µs+150µs, 1 ms and 20 ms).
587
588 **Calculation of difference density maps**
589 All F_o(light)-F_o(dark) difference maps were calculated using PHENIX[61] using the multi-
590 scaling option excluding amplitudes smaller than 3 σ and resolutions lower than 10 Å in the
591 anisotropy corrected data and phases of the refined neutral resting state.
592
593 **Structure determination and refinement of KR2 resting state**
594 The structure of the KR2 neutral resting state was solved using molecular replacement with
595 pdb 3x3c[2] as search model. The structure of the KR2 acidic resting state was refined directly
596 using the neutral model as a starting point. Structural refinements were done using PHENIX[61]
597 with iterative cycles of manual adjustments made in Coot[62].
598
599
600

601 **Data extrapolation**

602 Extrapolated data were calculated using the anisotropy corrected data and a linear
603 approximation as follows: $F_{Extra}=100/A\times(F_o(light)-F_o(dark))+F_o(dark)$, where A is the
604 activation level in percent, F_{Extra} are the extrapolated structure factor amplitudes. F_0(light)
605 was scaled to F_0(dark) prior to calculation of F_{Extra}. The activation level A (the percentage of
606 molecules that did neither stay in nor return to the dark state after the laser pulse) was
607 determined by calculating extrapolated maps with phases of the dark state and light data at
608 different activation levels in steps of 2 % in the calculation of F_{Extra}, until features of the dark
609 state appeared at the retinal. Based on this analysis, an activation level of 14 % was chosen
610 for extrapolated maps.

611

612 **Refinement of time-resolved states**

613 Negative amplitudes resulting from the extrapolation procedure were removed from the TR-
614 SFX data before model building and refinement. The models where manually adjusted to best
615 fit observed difference map features as well as extrapolated maps. For residues with multiple
616 conformations present in the resting state the prevalent conformation was chosen based on
617 electron density maps, followed by refinement in PHENIX[61]. Initial models were refined
618 against extrapolated data from all ten different time delays. Using a pairwise comparison at
619 all time delays (**compare Extended Data Fig. 4, b**) of structures based on their rmsd, in
620 combination with manual inspection of electron density maps and input from the time-
621 resolved spectroscopic data (**compare Fig. 1**) we identified structural transition points and
622 combined delays at 800 fs with 2 ps, 1ns with 16 ns and 30 µs with 150 µs to further
623 improve density maps and refinement statistics and model quality for the first three deposited
624 intermediates (**Extended Data Tab. 2**). In the final refinement of the two delays in the
625 millisecond regime restraints on sodium distance have been used. However, this only
626 marginally affected results, as the sodium atom close to the retinal binding pocket refined to a
627 distance of 2.4 Å to N112 and 2.7 Å to D251 with an average near identical to the 2.5 Å from
628 restrained refinement. A similar result was obtained within the second binding pocket where
629 the sodium atom refined to a distance of 2.4 Å to N106 and 2.5 Å to E11 with constrains and
630 2.4 Å to both residues without them.

631

632

633

634 **Time-resolved spectroscopy**

635 Crystals for the spectroscopic characterization have been prepared in a similar fashion as to
636 those used in the time-resolved SwissFEL experiments. A few microliters of crystals
637 immersed in LCP (lipidic cubic phase) were sandwiched between two BaF_2 windows and
638 sealed with vacuum paste immediately after extrusion to prevent drying[63]. Similar to our
639 previous studies[64,65], KR2 solubilized in 0.02% DDM, 0.004% CHS with 100 mM Tris pH
640 8.0, 150 mM NaCl, was dried from a concentrated protein solution on a BaF_2 window. The
641 dried film was rehydrated via the vapor phase generated by a glycerol/water mixture in a 3:2
642 ratio and sealed with a second window using vacuum grease.

643 Time-resolved IR experiments were recorded on a home-built spectrometer based on tunable
644 Quantum Cascade Lasers (QCLs) as described in[42]. We traced transient absorption changes in
645 the frequency range of 1510-1690 cm^{-1} in steps of 2 cm^{-1} for crystals and 1 cm^{-1} for protein
646 film across the time range of 5 ns - 200 ms. For experiments on rehydrated KR2 films in KCl
647 (used for comparison in **Extended Data Fig. 2**) the lower time resolution of rapid-scan
648 spectroscopy was sufficient.

649 The repetition rate was set to 2 Hz and each kinetic was averaged 25 times. After reaching
650 1690 cm^{-1} the scanning direction was reversed and the two datasets were merged accounting
651 for possible protein bleaching. The frequency-doubled emission of a Q-switched Nd:YAG
652 (Neodymium Yttrium Aluminum Garnet, Minilite; Amplitude, Pessac, France) laser emitting
653 at 532 nm was used for photoactivation with an energy density set to ~3 mJ/cm^2.

654 Absorption changes in the visible were recorded using a commercial flash photolysis setup
655 (LKS70; Applied Photophysics, Leatherhead, UK) essentially as described in[64]. The
656 photoreaction was induced by a short laser pulse emitted by a Nd:YAG laser (Quanta-Ray;
657 Spectra-Physics, Santa Clara, USA), which drives an optical parametric oscillator tuned to
658 523 nm with an energy density of ~3 mJ/cm^2. Transients were recorded from 380 to 650 nm
659 in 10 nm steps omitting the wavelength around the exciting laser pulse due to light scattering
660 (i.e. 510-550 nm). Each trace was recorded 10x with a repetition rate of 2 Hz and
661 subsequently averaged.

662 Time-resolved step-scan and rapid-scan FTIR experiments on KR2 films were conducted
663 using a Vertex 80v spectrometer (Bruker Optics, Ettlingen, Germany). Excitation laser source
664 was the same as for the QCL measurements with a repetition rate of 2 Hz for the step-scan
665 mode. In the case of rapid-scan experiments a slower repetition rate of 0.018 Hz taking
666 account for the slower photocycle of KR2 in the presence of KCl.

667 We reconstructed the recorded data by applying singular value decomposition (SVD). Kinetic
668 analysis was done by fitting the data to a model consisting of a unidirectional sequence of
669 states. This yields a concentration profile of the involved and spectroscopically observable
670 states over the course of our measurement[65].
671
672 **Hybrid quantum mechanics/molecular mechanics (QM/MM) calculations**
673 Crystallographic coordinates from TR-SFX were used as the initial input for the hybrid
674 quantum mechanics/molecular mechanics (QM/MM) calculations[66]. A subsystem of the
675 protein was chosen and treated using a quantum chemical method (QM region), while the
676 remaining part was treated using a classical force-field (MM region), namely AMBER
677 ff14SB[67]. The QM region includes the retinal chromophore, the side chain of K255, and side
678 chains of residues D116, N112, and D251. The link atom was placed at the QM/MM
679 boundary between the Cα-Cβ atoms of the amino acids. To test the effect of sodium binding
680 we included either a sodium ion or a water in the QM region of the 1 ms structure.
681 The geometry optimization was performed at the B3LYP/cc-pVDZ/AMBER level of theory.
682 In these simulations, the protein backbone position was fixed to the crystallographic
683 structure, whereas the QM region and side chains of amino acids within the 5 Å region of the
684 retinal protonated Schiff base in the MM region was relaxed. Resolution of identity for
685 Coulomb integrals (RI-J) and chain of sphere approximation for the Exchange integrals were
686 applied (RIJCOSX)[68]. Corrections for dispersion effect was included with D3/B-J damping
687 variant[69]. The calculation of vertical excitation energies uses the simplified TD-DFT
688 method[70] developed by Grimme and co-workers at CAM-B3LYP/cc-pVTZ level of theory.
689 All the QM/MM calculations were performed with quantum chemistry package Orca
690 interfaced with DL_POLY module of ChemShell[71] for the force-field.
691
692
693
694
695

696 **Extended Data Items available for this paper.**

697 Extended Data Figures 1-6

698 Extended Data Tables 1-2

699 Videos 1-2

700

701

702

703 **Extended Data Items**

704
705
706 **Extended Data Fig. 1: TR-SFX sample preparation scheme and characterization. (a)**
707 Two lipidic phases, the first containing KR2 crystals where the acidic buffer had been
708 washed away and the second containing soaking buffer, were mixed through a three-way
709 coupler[41]. The sodium concentration was adjusted to 150 mM and tests with litmus paper
710 indicate a pH close to 8 in the final mixture. **(b)** Left column: Crystals after TR-SFX sample
711 preparation with varying Tris buffers with pH values from 7.0 to 9.0. Right column: KR2 in
712 200 mM Tris, 150 mM NaCl, 0.02% DDM, 0.004% CHS solution with varied pH of Tris
713 buffer. Note that crystals grown in LCP reach red color after mixing with Tris pH 9.0,
714 whereas the solution reaches red color at pH 8.0. Likely this shift is due to residual buffering
715 capacity from the original crystallization conditions as confirmed by a litmus paper test. **(c)**
716 Size distribution of crystals determined by microscopic inspection after TR-SFX sample
717 preparation. (**d**) Microscopic picture of KR2 crystals grown at acidic pH and in absence of
718 NaCl, after washing out the crystallization buffer, the TR-SFX sample prepared via the
719 procedure shown in (**a**), and LCP with KR2 crystals soaked directly as control. The color
720 change upon increasing pH has been confirmed in five independent experiments. **(e)**
721 Overview of TR-IR traces and absorption spectra obtained from blue KR2 crystals in the
722 original acidic crystallization condition, red crystals prepared in analogy to the TR-SFX
723 experiment and in hydrated film at pH 8 in presence of sodium chloride. The corresponding
724 lower panels show a kinetic analysis of KR2 intermediates obtained by singular value
725 decomposition (SVD) of the spectroscopic data. Time constants are given in brackets. Under
726 acidic conditions, KR2 in crystals exhibits an accelerated photocycle. In treated crystals on
727 the other hand the critical deprotonation step in the M intermediate is occurring with similar
728 kinetics as in purified KR2. **(f, g)** Detailed view of the retinal binding pocket in the serial
729 crystallographic room temperature structures of KR2 obtained from **(f)** blue crystals at acidic
730 pH and **(g)** red crystals after soaking in neutral pH and NaCl. Critical hydrogen bonds with a
731 distance ≤ 3.2 Å are indicated by black dotted lines. Arrows signify the distance of the SB to
732 w406 and the D116 counterion. In neutral conditions w406 has shifted away from the SB
733 while D116 and N112 are now within hydrogen bonding distance. The resulting change in
734 electrostatic environment is responsible for the color change as reported previously[2].
735
736
737
738 **Extended Data Fig. 2: Spectroscopic analysis of sodium binding mode.** Time-resolved
739 infrared spectra from KR2 microcrystals at (**a**) pH 8 and at (**b**) pH 4 recorded with tunable
740 Quantum Cascade Lasers as described in[42]. The maximum concentration of the O
741 intermediate is reached at around 1-20 ms after pulsed excitation at pH 8 and is characterized
742 by specific marker bands that are absent at pH 4, in particular the C=C stretching vibrational
743 band of retinal at 1516 cm^{-1} of the O state. The band at 1688 cm^{-1} has previously been
744 suggested to originate from the C=O stretching mode due to sodium binding to an asparagine
745 residue, presumably N112[43]. The band at 1554 cm^{-1} is tentatively assigned to the asymmetric
746 stretching vibration of a carboxylate that rises upon binding of a sodium ion in bidendate or
747 pseudo-bridging fashion where one of the carboxylate oxygens is interacting with another
748 partner[44,45]. For a detailed analysis of the ligation, the corresponding symmetrical mode needs
749 to be assigned as the frequency difference between the COO^- asymmetric and symmetric
750 stretch is dependent on the mode of sodium ligation[46,47]. (**c**) O(like)-KR2 (ground state)
751 difference spectra recorded under different conditions. Spectra have been scaled to the
752 ground-state bleaching band measured between 1530 and 1540 cm^{-1}. It is well-established

753 that KR2 operates exclusively as a sodium pump at neutral pH and in the presence of sodium
754 ions. KR2 acts as proton pump in the presence of KCl but has no (known) function at pH
755 4[1,28]. It is evident that the band at 1688 cm^{-1} is most pronounced if sodium is pumped, which
756 supports the assignment to the C=O stretching vibration of N112 upon binding of sodium. (**d**)
757 Time traces of the ethylenic stretch of the O state vibrating at 1518 cm^{-1} and the two
758 candidate vibrational bands at 1420 cm^{-1} and 1392 cm^{-1} of the symmetric carboxylate
759 stretching vibration. The band at 1420 cm^{-1} exhibits similar kinetic behaviour as the one at
760 1518 cm^{-1}. Hence, the former vibrational band is tentatively assigned as the symmetrical
761 mode that relates to the asymmetrical vibration at 1554 cm^{-1} of deprotonated D251 upon
762 ligation of a sodium ion. The difference in frequency of the symmetric and asymmetric
763 modes is with 135 cm^{-1} at the edge of binding in bidentate to pseudobridging mode of model
764 compounds[2,4,5]. This indicates that the two oxygen of D251 are not equidistant to the sodium
765 ion. Such asymmetric ligation is expected in the heterogenous environment of the protein
766 interior as documented by our X-ray structures in the millisecond regime.
767
768
769
770 **Extended Data Fig. 3: Comparison of data truncation schemes and changes in retinal**
771 **over time. (a)** The top panels show F_o-F_c simulated annealing omit maps of the resting state
772 at 4 σ. No truncation (left) shows the map using all data up to 1.6 Å resolution along a*, b*
773 and c*. Spherical truncation (middle) shows the map using all data up to 2.2 Å resolution
774 along a*, b* and c*. Anisotropic truncation (right) shows the map using data up to 2.3 Å, 2.2
775 Å and 1.6 Å resolution along a*, b* and c*, respectively, as truncated by the staraniso
776 server[48]. The lower panels show the F_o(light)-F_o(dark) difference density maps of the 1 ms
777 time delay at the region around retinal and V117 at 3 σ. The structure is shown as sticks
778 (resting state salmon and 1 ms refined structure in cyan). No truncation (left) shows the map
779 using all data up to 1.6 Å resolution. Spherical truncation (middle) shows the map using all
780 data up to 2.2 Å resolution. Anisotropic truncation (right) shows the map using data up to 1.6
781 Å resolution in c* as truncated by the staraniso server. Overall the truncated data processed
782 by result in better electron density maps (both for $2F_o$-F_c maps and F_o(light)-F_o(dark)
783 difference maps) with finer features being resolved. This effect is likely because noise along
784 the missing directions is removed when compared to no truncation, while retaining the high-
785 resolution data along c* when compared to spherical truncation. (**b**) The panels show the
786 evolution of electron density around the retinal chromophore over time. Retinal and K255 of
787 the refined structures are shown as sticks and the electron density is displayed around them
788 (blue mesh, 2σ). The dark panel on the top shows the original $2F_o$-F_c electron density map
789 and the panels below show extrapolated $2F_{extra}$-F_c maps. The extrapolated maps allow to
790 follow retinal isomerization in detail. In the dark state, the middle section or the retinal
791 polyene chain is slightly bent downwards. In the picoseconds range, the isomerization is
792 completed and the polyene appears to be straightened. In our ultrafast data, we did not
793 observe retinal with a pronounced twist in the C13=C14 bond as in bR, with retinal in KR2
794 reaching a near planar 13-*cis* conformation much earlier along the activation pathway. In the
795 time delays from nanoseconds to milliseconds, the electron density reveals a bend in the
796 retinal molecule resulting from two planes which are twisted against each other. While the
797 exact dihedral angles cannot be refined realistically based on the extrapolated data, the bend
798 seems to originate from the C9=C10-C11=C12 dihedral angle as suggested for the L, M and
799 O intermediates based on time-resolved FTIR[18] and resonance Raman spectroscopy[33]. After
800 20 milliseconds, a definite conclusion concerning the retinal isomer is difficult. The
801 extrapolated maps suggest that a fraction of the retinal molecules may have already re-
802 isomerized to the all-*trans* conformation, while it is still bend sideward.

Extended Data Fig. 4: Experimental setup and evolution of structural changes over time. (a) KR2 crystals were extruded in a stream of LCP from a high viscosity injector. At the interaction point, the crystals were pumped with 575 nm femtosecond laser pulses before probing for structural changes with near parallel 12 keV XFEL pulses arriving from SwissFEL with a specific time delay Δt. The diffraction patterns are collected with a Jungfrau 16 M detector in a series of four light-activated patterns and one dark pattern, for which the visible pump laser had been blocked. To reduce background through diffuse scattering of XFEL radiation in air, the experimental chamber was pumped down to 100-200 mbar while the residual air is replaced by helium. (**b**) The evolution of structural changes in KR2 over time can be followed in a matrix of root-mean-square deviations (rmsd) between all protein and retinal atoms (total of 2703) in individual KR2 structural snapshots. The numerical rmsd values have been determined using the program pymol and are colored in a blue-white-red gradient. The black boxes highlight time delays where we combined data based on manual inspection of electron density maps and the evolution of photo intermediates in KR2 crystals determined by TR-IR spectroscopy. The approach was inspired by a recently published tool for visualizing protein motions in time-resolved crystallography[49] but relies on refined atom positions instead of electron density changes. **(c)** Difference electron density maps (F_o(light) - F_o(dark), negative density in gold and positive density in blue, contoured at 4 σ and shown together with the KR2 resting state) obtained at the indicated time delays. The first panel is included as a control and shows difference electron density obtained from 50k patterns collected with laser off and 100k images from dark patterns obtained by the 4 light / 1 dark cycle used during the TR-SFX data collection. For orientation important residues discussed in the main text are shown as sticks.

Extended Data Fig. 5: Comparison of monomeric and pentameric KR2 structures. Overall the structures at neutral pH reported in this work (left), Kato *et al.*[2], (middle) and Kovalev *et al.*[20] (right) are very similar (rmsd of Cα atoms of 0.30 and 0.72 Å) with the position of residues and hydrogen bonding pattern (lower insets, black dotted lines, defined as distance ≥ 3.2 Å) in the binding pocket well preserved. Depending on conditions, the pocket in the pentameric structure can adopt the shown extended conformation. Here N112 is rotated out into the interaction interface between two KR2 protomers (colored red) and the space is filled with water molecules. Since the pentameric resting state can adopt a more open conformation in the Schiff base region[3], we cannot exclude that the electrostatic gate does not fully open in our crystals formed from monomeric KR2 (see main text). However, a yet unpublished steady-state structure of pentameric KR2 under continuous illumination (6XYT, Gordeliy group, IBS Grenoble) shows N112 rotated back into the binding pocket in a conformation very similar to our time-resolved millisecond states. As the retinal is modelled in the *trans* configuration the structure may represent a later intermediate compared to what we observe. The opening along the retinal (calculated by the program Caver[40]) in our 30µs+150µs structure is 1.4 Å, which is very close to the 1.9 Å needed for a sodium ion to pass. Stable structural intermediates that accumulate in time-resolved studies of molecule ensembles do not necessarily reveal all functional states[34] and it seems reasonable that a gate should only form when sodium is in close proximity to the SB. This would allow fast transfer of sodium to the extracellular side upon deprotonation. The gate would then collapse immediately upon sodium binding on the extracellular side, coinciding with reprotonation of the SB. Such a mechanism would efficiently prevent sodium back leakage. Differences in the position of N112 between the monomer and pentameric resting states could furthermore explain the long-range effects of mutations in the oligomerization interface on the photocycle[17] and sodium pumping efficiency[1,17,20].

852 **Extended Data Fig. 6: Comparison of ion binding sites in selected members of the**
853 **rhodopsin family and QM/MM simulations.** (**a**) Sodium binding site in *Krokinobacter*
854 *eikastus* rhodopsin 2 (KR2, this work), (**b**) chloride binding site in the related bacterial pump
855 *Nonlabens marinus* rhodopsin 3 (NM-R3, pdb code 5G28[50]), (**c**) protonated Schiff base in
856 bacteriorhodopsin (bR, pdb code 6RQP[26]), (**d**) chloride binding site in halorhodopsin (HR,
857 pdb code 1E12[51]). The retinal chromophore together with selected interactions and amino
858 acid side chains are shown as dotted lines or sticks. Besides overall similarity in ion binding
859 between bacteria and archea, the suggested binding site in KR2 is in line with quantum
860 chemical calculation of absorbance changes upon sodium binding. The QM/MM optimized
861 geometry of (**e**) the resting state and the 1 ms structure with (**f**) water or (**g**) sodium bound to
862 N112, D251. (**h**) Comparison of the absorption shifts of the states measured in UV-Vis
863 difference spectroscopy with the calculated QM/MM excitation wavelengths. Absolute
864 values are given in brackets. Extent and location of structural changes in (**i**) KR2 at 20 ms
865 and (**j**) bR at 15 ms after activation (blue to red gradient and ribbon width indicate rmsd to
866 the resting state, bR coordinates taken from[26]). The light-driven pumping against a
867 concentration gradient is achieved with smaller conformational changes in the order of 1-2 Å
868 in sodium pumping KR2 compared to the more elusive protons pumped by bR[24,26]. The
869 translocation path for sodium and protons (indicated by arrows), however, is similar for both
870 proteins and includes three critical sites (for reviews on bR structural dynamics and activation
871 mechanism, see ref[52] and ref[53], respectively). Close to the water-filled cavity on the
872 cytoplasmic side of KR2, Q123 of the NDQ motif is the most likely location where the
873 sodium ion is losing its water coordination shell. The position is analogous to D96 of the
874 DTD motif in bR, which is the primary donor for reprotonation at the end of the pumping
875 cycle. The second critical site is formed by D116, N112 and D251 which correspond to D85,
876 T89 and D212 in bR and coordinate sodium and proton transport in the SB region. The role
877 of R109 in switching from water to sodium binding in KR2 is analogous in position and
878 function to R82, which is regulating the transfer of protons towards the release group in bR.
879 The proton release group in bR is formed by E194 and E204 with the position overlapping
880 well with the second sodium binding site between E11, N106 and E160 at the extracellular
881 side of KR2. Beside these similarities, the sequence of events is clearly different between the
882 two outward ion pumps. Whereas light-driven pumping in bR starts with (1) a prebound
883 proton followed by (2) release and (3) reloading. In KR2 the process is shifted in sequence
884 with (1) entry, (2) binding and (3) release with a corresponding adaptation of the photocycle
885 intermediates. The similar ion binding modes between bacteria and archea together with how
886 retinal isomerization is used to drive them, provides an exciting example for the evolutionary
887 economy of nature. The adaptation of this common leitmotif is particularly interesting in the
888 case of KR2 where substrate binding has been shifted from the stable resting state into a
889 transient intermediate.
890

891
892
893 **Extended Data Table 1:** X-ray statistics.
894
895
896 **Extended Data Table 2:** Refinement statistics. *Data are anisotropic, see extended statistics
897 Table 1 and Materials and Methods.
898
899
900 **References Methods and Extended Data Files**
901

902 41. James, D. *et al.* Improving High Viscosity Extrusion of Microcrystals for Time-
903 resolved Serial Femtosecond Crystallography at X-ray Lasers. *J Vis Exp* (2019).
904 doi:10.3791/59087
905 42. Schultz, B.-J., Mohrmann, H., Lórenz-Fonfría, V. A. & Heberle, J. Protein dynamics
906 observed by tunable mid-IR quantum cascade lasers across the time range from 10ns to
907 1s. *Spectrochim Acta A Mol Biomol Spectrosc* **188,** 666–674 (2018).
908 43. Balashov, S. P. *et al.* Light-driven Na(+) pump from Gillisia limnaea: a high-affinity
909 Na(+) binding site is formed transiently in the photocycle. *Biochemistry* **53,** 7549–
910 7561 (2014).
911 44. Noguchi, T., Ono, T.-A. & Inoue, Y. Direct detection of a carboxylate bridge between
912 Mn and Ca^{2+} in the photosynthetic oxygen-evolving center by means of Fourier
913 transform infrared spectroscopy. *Biochim. Biophys. Acta* **1228,** 189–200 (1995).
914 45. Nara, M. *et al.* Infrared studies of interaction between metal ions and Ca(2+)-binding
915 proteins. Marker bands for identifying the types of coordination of the side-chain
916 COO- groups to metal ions in pike parvalbumin (pI = 4.10). *FEBS Lett.* **349,** 84–88
917 (1994).
918 46. Nara, M., Morii, H. & Tanokura, M. Coordination to divalent cations by calcium-
919 binding proteins studied by FTIR spectroscopy. *Biochim. Biophys. Acta* **1828,** 2319–
920 2327 (2013).
921 47. Furutani, Y., Murata, T. & Kandori, H. Sodium or lithium ion-binding-induced
922 structural changes in the K-ring of V-ATPase from Enterococcus hirae revealed by
923 ATR-FTIR spectroscopy. *J. Am. Chem. Soc.* **133,** 2860–2863 (2011).
924 48. Tickle, I. J. *et al.* Staraniso. *staraniso.globalphasing.org* Available at:
925 http://staraniso.globalphasing.org/cgi-bin/staraniso.cgi. (Accessed: 3rd April 2020)
926 49. Wickstrand, C. *et al.* A tool for visualizing protein motions in time-resolved
927 crystallography. *Structural Dynamics (Melville, N.Y.)* **7,** 024701 (2020).
928 50. Kim, K. *et al.* Crystal structure and functional characterization of a light-driven
929 chloride pump having an NTQ motif. *Nature Communications* **7,** 12677 (2016).
930 51. Kolbe, M., Besir, H., Essen, L. O. & Oesterhelt, D. Structure of the light-driven
931 chloride pump halorhodopsin at 1.8 A resolution. *Science* **288,** 1390–1396 (2000).
932 52. Wickstrand, C. *et al.* Bacteriorhodopsin: Structural Insights Revealed Using X-Ray
933 Lasers and Synchrotron Radiation. *Annual review of Biochemistry* (2019).
934 doi:10.1146/annurev-biochem-013118-111327
935 53. Gerwert, K., Freier, E. & Wolf, S. The role of protein-bound water molecules in
936 microbial rhodopsins. *Biochim. Biophys. Acta* **1837,** 606–613 (2014).
937 54. Weierstall, U. *et al.* Lipidic cubic phase injector facilitates membrane protein serial
938 femtosecond crystallography. *Nature Communications* **5,** 3309 (2014).
939 55. Claesson, E. *et al.* The primary structural photoresponse of phytochrome proteins

940 captured by a femtosecond X-ray laser. *bioRxiv* doi:10.1101/789305
941 56. White, T. A. *et al.* CrystFEL: a software suite for snapshot serial crystallography. *J*
942 *Appl Crystallogr* **45,** 335–341 (2012).
943 57. White, T. A. *et al.* Recent developments in CrystFEL. *J Appl Crystallogr* **49,** 680–689
944 (2016).
945 58. Gevorkov, Y. *et al.* XGANDALF - extended gradient descent algorithm for lattice
946 finding. *Acta Crystallogr A Found Adv* **75,** 694–704 (2019).
947 59. Ginn, H. M. *et al.* TakeTwo: an indexing algorithm suited to still images with known
948 crystal parameters. *Acta Crystallogr D Struct Biol* **72,** 956–965 (2016).
949 60. Berman, H., Henrick, K. & Nakamura, H. Announcing the worldwide Protein Data
950 Bank. *Nat. Struct. Biol.* **10,** 980 (2003).
951 61. Adams, P. D. *et al.* PHENIX: building new software for automated crystallographic
952 structure determination. *Acta Crystallogr. D Biol. Crystallogr.* **58,** 1948–1954 (2002).
953 62. Emsley, P. & Cowtan, K. Coot: model-building tools for molecular graphics. *Acta*
954 *Crystallogr. D Biol. Crystallogr.* **60,** 2126–2132 (2004).
955 63. Heberle, J., Büldt, G., Koglin, E., Rosenbusch, J. P. & Landau, E. M. Assessing the
956 functionality of a membrane protein in a three-dimensional crystal. *J. Mol. Biol.* **281,**
957 587–592 (1998).
958 64. Lórenz-Fonfría, V. A. *et al.* Transient protonation changes in channelrhodopsin-2 and
959 their relevance to channel gating. *Proc. Natl. Acad. Sci. U.S.A.* **110,** E1273–81 (2013).
960 65. Ehrenberg, D. *et al.* The Two-Photon Reversible Reaction of the Bistable Jumping
961 Spider Rhodopsin-1. *Biophys. J.* **116,** 1248–1258 (2019).
962 66. Senn, H. M. & Thiel, W. QM/MM methods for biomolecular systems. *Angew. Chem.*
963 *Int. Ed. Engl.* **48,** 1198–1229 (2009).
964 67. Maier, J. A. *et al.* ff14SB: Improving the Accuracy of Protein Side Chain and
965 Backbone Parameters from ff99SB. *J Chem Theory Comput* **11,** 3696–3713 (2015).
966 68. Kossmann, S. & Neese, F. Efficient Structure Optimization with Second-Order Many-
967 Body Perturbation Theory: The RIJCOSX-MP2 Method. *J Chem Theory Comput* **6,**
968 2325–2338 (2010).
969 69. Grimme, S., Ehrlich, S. & Goerigk, L. Effect of the damping function in dispersion
970 corrected density functional theory. *J Comput Chem* **32,** 1456–1465 (2011).
971 70. Grimme, S. A simplified Tamm-Dancoff density functional approach for the electronic
972 excitation spectra of very large molecules. *J Chem Phys* **138,** 244104 (2013).
973 71. Metz, S., Kästner, J., Sokol, A., Keal, T. & Sherwood, P. ChemShell—a modular
974 software package for QM/MM simulations. *Wires computational molecular science* **4,**
975 (2014).
976

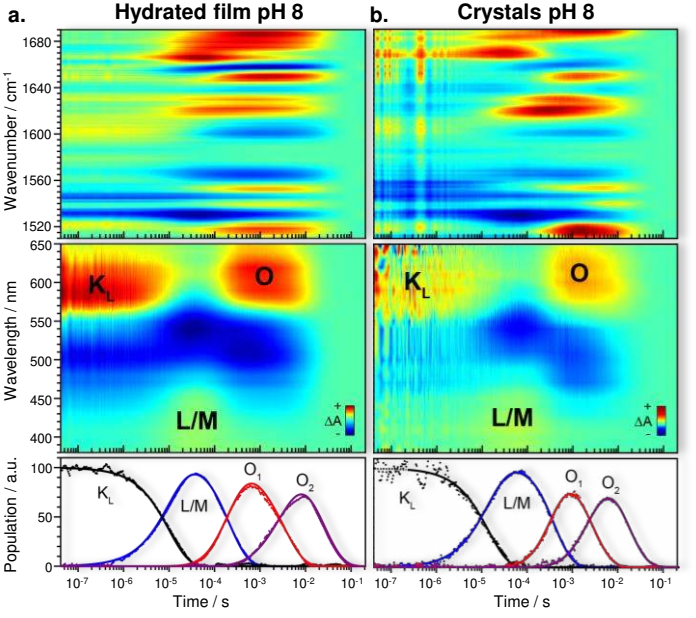
a.
Hydrated film pH 8
b.
Crystals pH 8
Wavenumber / cm-1
1680
1640
1600
1560
1520
Wavelength / nm
650
600
550
500
450
400
K_L
O
L/M
ΔA
+
-
Population / a.u.
100
50
0
K_L
L/M
O_1
O_2
10-7
10-6
10-5
10-4
10-3
10-2
10-1
Time / s

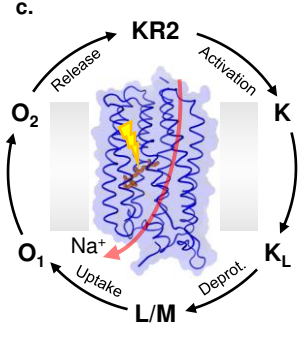
c.
KR2
Release
Activation
K
K_L
Deprot.
L/M
Uptake
O_1
O_2
Na+

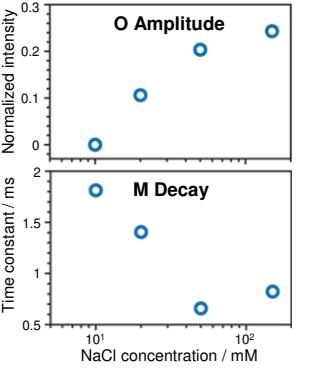
d.
O Amplitude
Normalized intensity
0.3
0.2
0.1
0
M Decay
Time constant / ms
2
1.5
1
0.5
10^1
10^2
NaCl concentration / mM

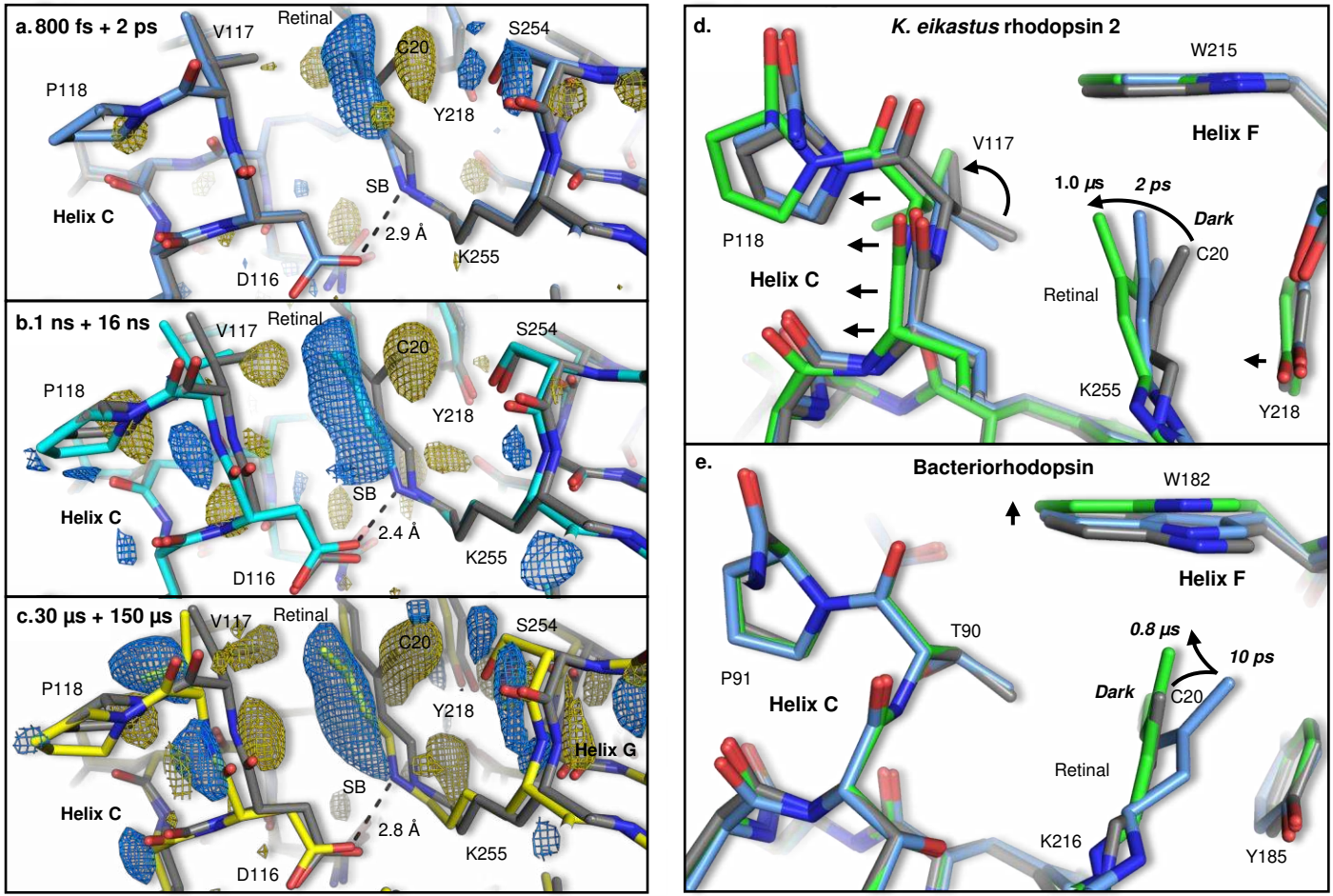
a. 800 fs + 2 ps
V117
Retinal
C20
S254
P118
Y218
SB
Helix C
2.9 Å
K255
D116
b. 1 ns + 16 ns
V117
Retinal
C20
S254
P118
Y218
SB
Helix C
2.4 Å
K255
D116
c. 30 µs + 150 µs
V117
Retinal
C20
S254
P118
Y218
Helix G
SB
Helix C
2.8 Å
K255
D116
d.
K. eikastus rhodopsin 2
W215
Helix F
V117
1.0 µs
2 ps
Dark
P118
C20
Helix C
Retinal
K255
Y218
e.
Bacteriorhodopsin
W182
Helix F
T90
0.8 µs
10 ps
P91
Dark
C20
Helix C
Retinal
K216
Y185

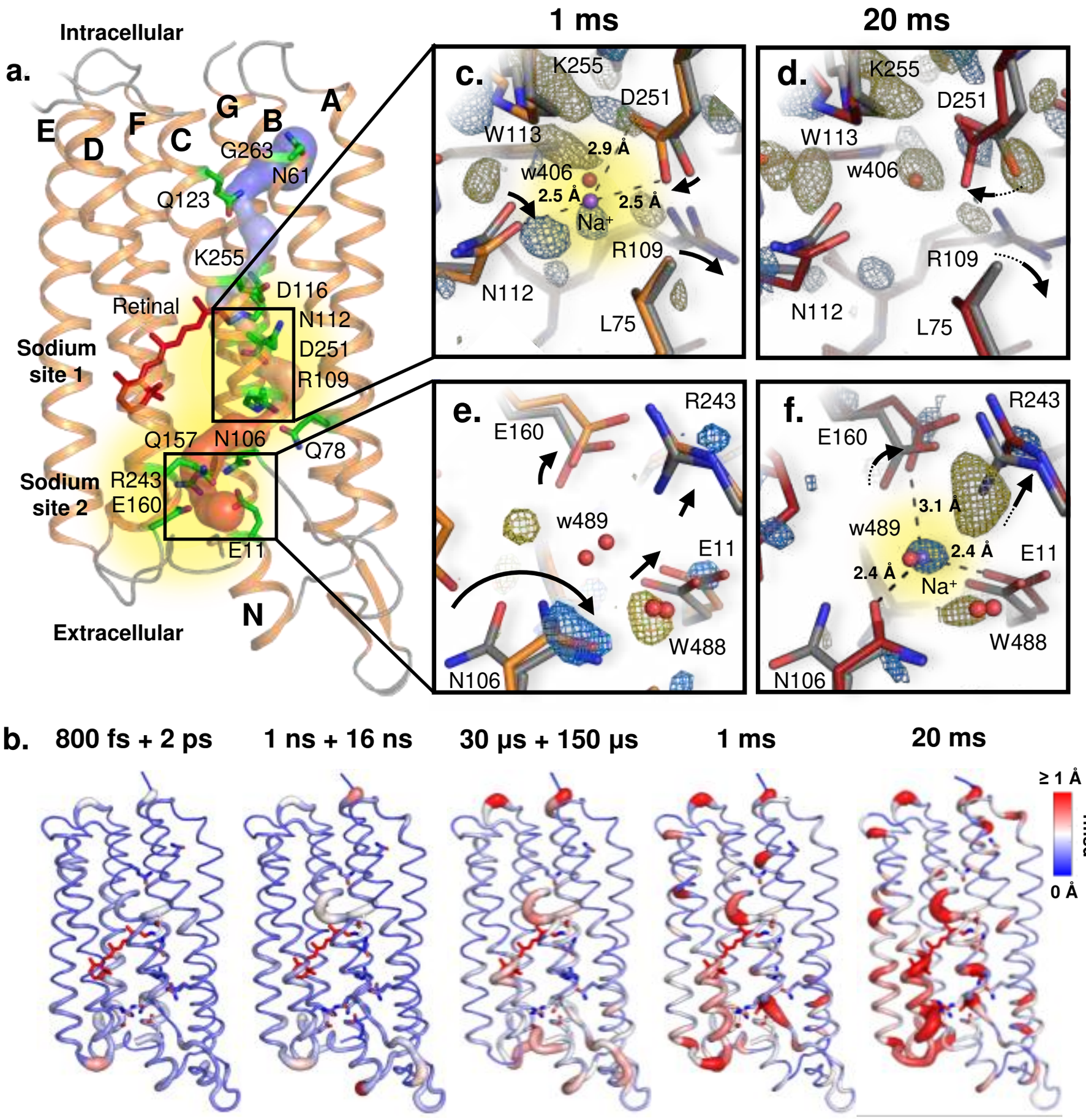
a.
Intracellular
E
D
F
C
G
B
A
G263
N61
Q123
K255
D116
Retinal
N112
D251
R109
Sodium site 1
Q157
N106
Q78
Sodium site 2
R243
E160
E11
N
Extracellular
1 ms
20 ms
c.
K255
D251
W113
2.9 Å
w406
2.5 Å
2.5 Å
Na+
R109
N112
L75
d.
K255
D251
W113
w406
R109
N112
L75
e.
E160
R243
w489
E11
W488
N106
f.
E160
R243
3.1 Å
w489
2.4 Å
E11
2.4 Å
Na+
W488
N106
b.
800 fs + 2 ps
1 ns + 16 ns
30 µs + 150 µs
1 ms
20 ms
≥ 1 Å
rmsd
0 Å

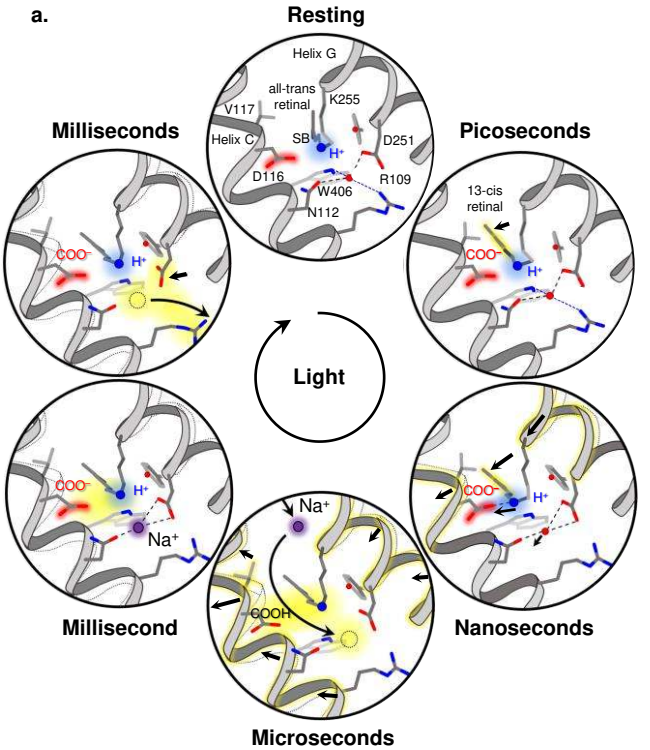

QM/MM optimized structures of the 1 ms intermediate

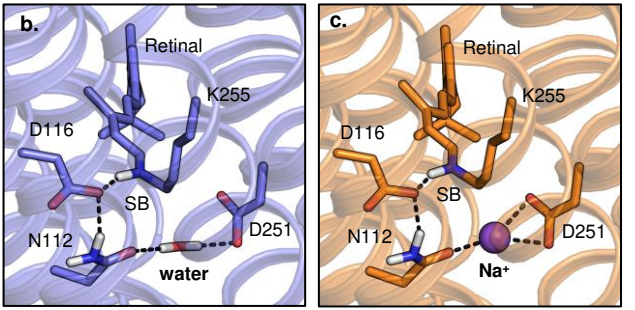

absorbance shift vs resting state:
-11 nm (blue)

absorbance shift vs resting state:
+55 nm (red)

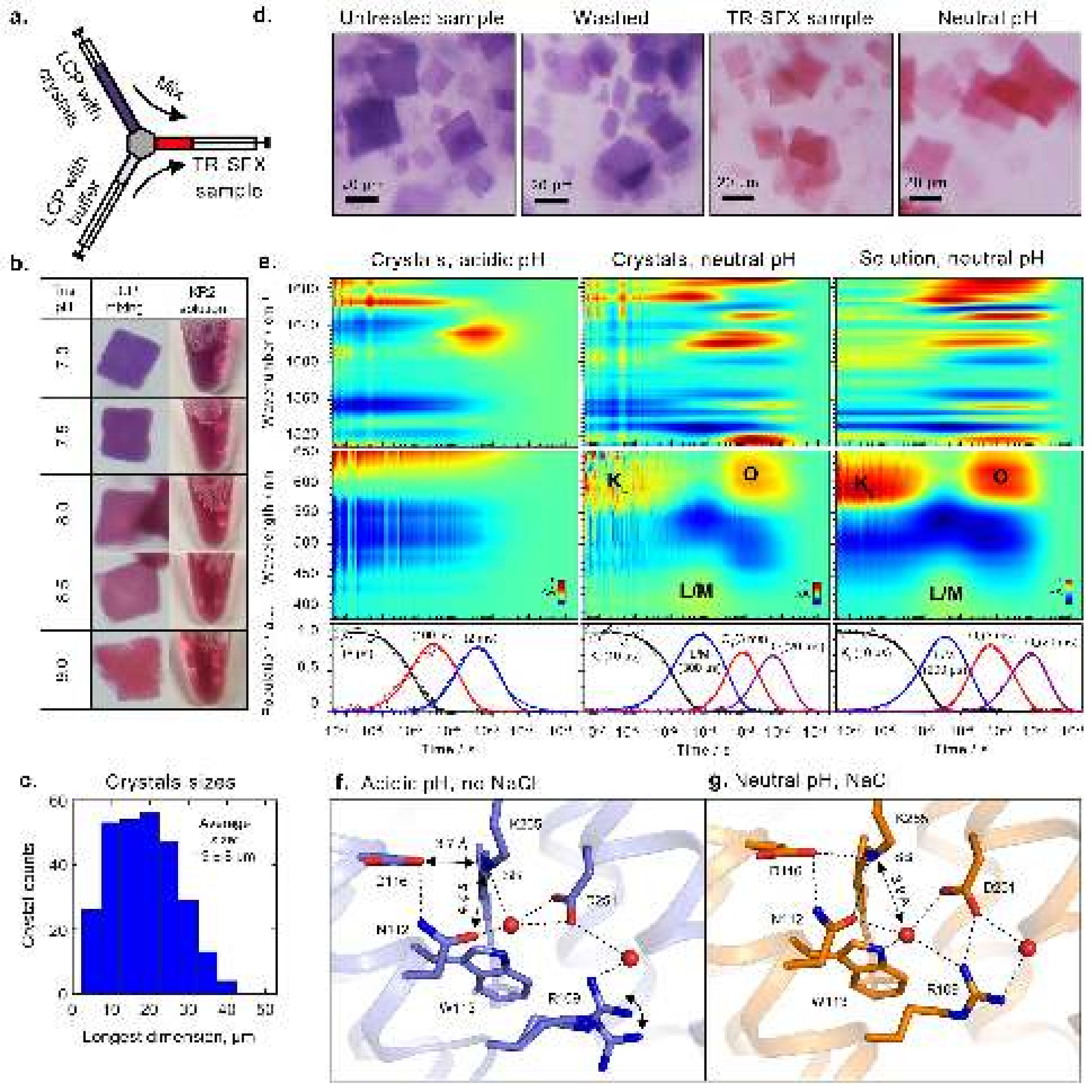
a.
LCP with crystals
Mix
LCP with buffer
TR-SFX sample
b.
pH
KP2 solution
7.0
7.5
8.0
8.5
9.0
c.
Crystals sizes
Crystal counts
Longest dimension, μm
d.
Untreated sample
Washed
TR-SFX sample
Neutral pH
e.
Crystals, acidic pH
Crystals, neutral pH
Solution, neutral pH
K
O
L/M
Time, s
f. Acidic pH, no NaCl
g. Neutral pH, NaCl
R255
N112
W113
R109
D251

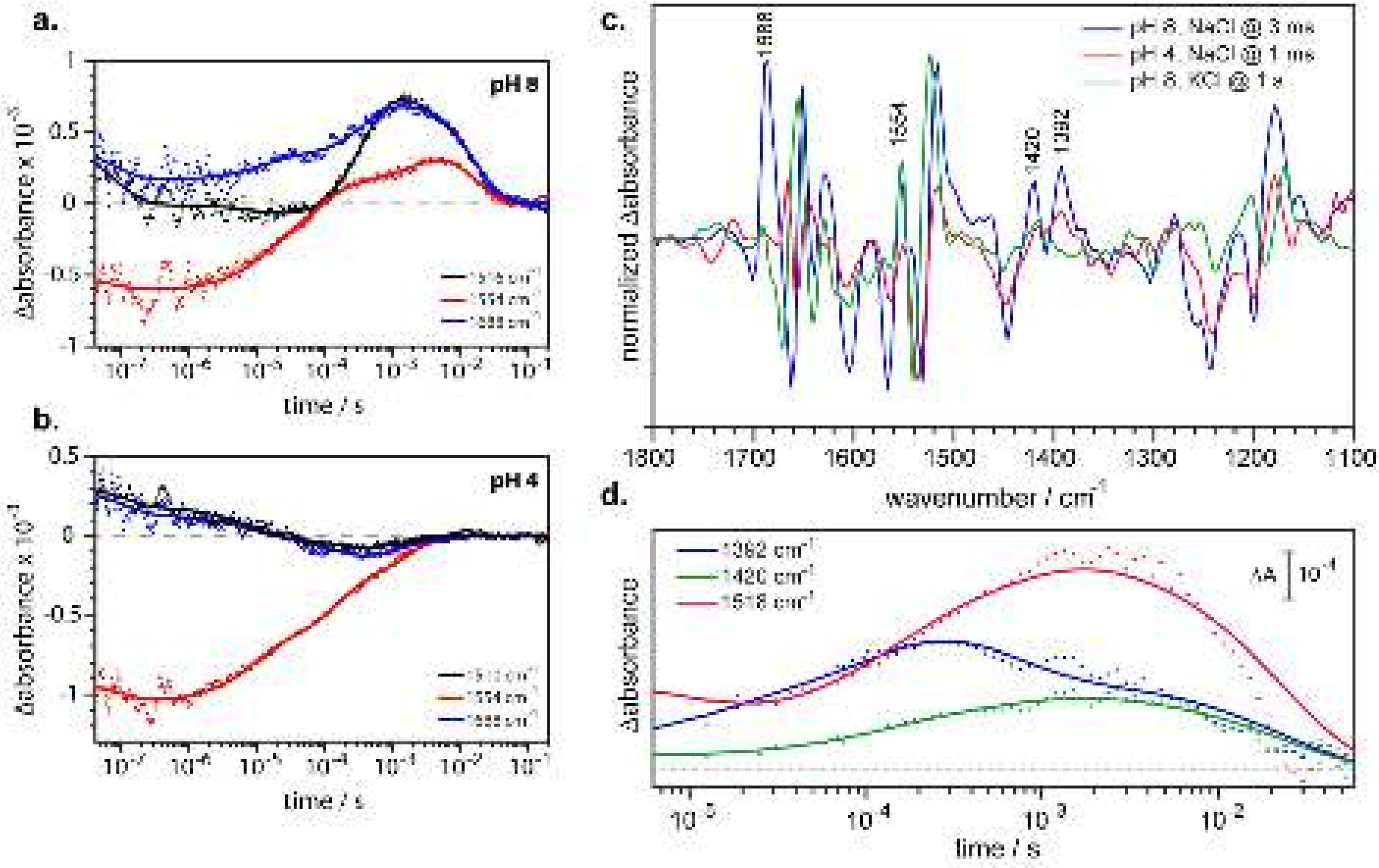
a.
pH 8
Δabsorbance x 10⁻³
time / s
b.
pH 4
Δabsorbance x 10⁻³
time / s
c.
pH 8, NaCl @ 3 ms
pH 4, NaCl @ 1 ms
pH 8, KCl @ 1 s
1688
1554
1420
1392
normalized Δabsorbance
wavenumber / cm⁻¹
d.
1392 cm⁻¹
1420 cm⁻¹
1518 cm⁻¹
ΔA 10⁻⁴
Δabsorbance
time / s

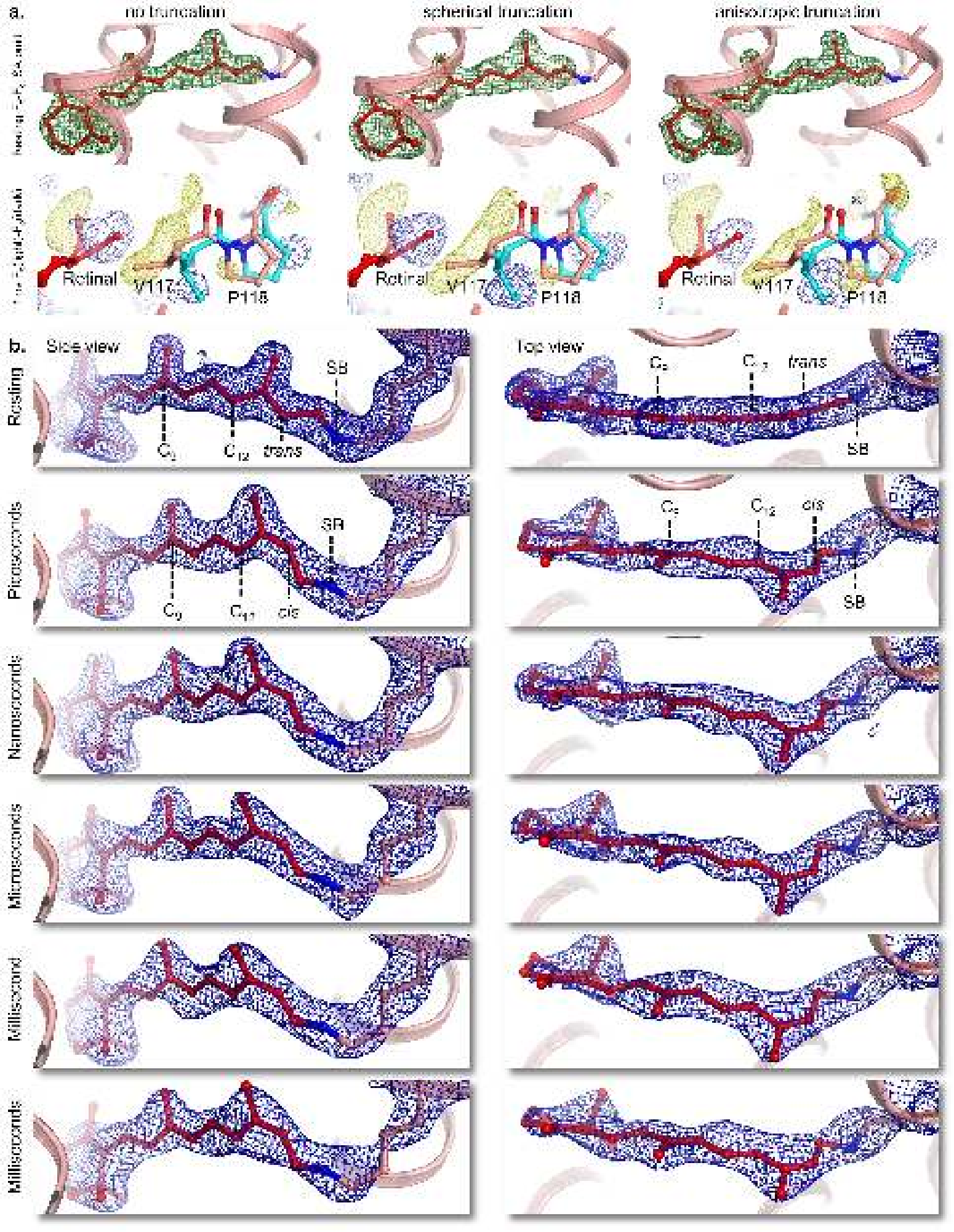
a.
no truncation
spherical truncation
anisotropic truncation
Retinal
W117
P118
b.
Resting
Picoseconds
Nanoseconds
Microseconds
Millisecond
Milliseconds
Side view
Top view
SB
trans
cis

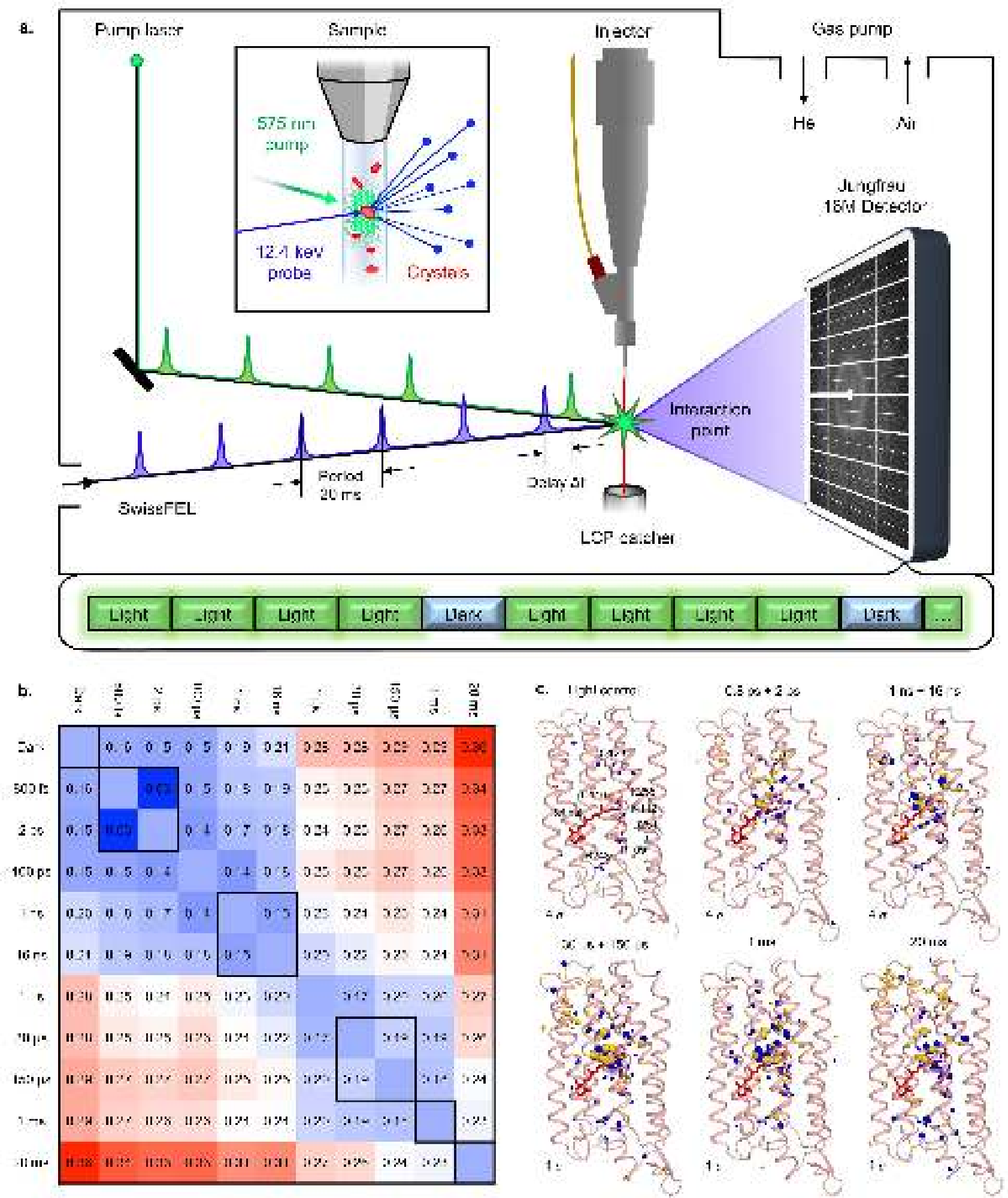
a.
Pump laser
Sample
Injector
Gas pump
He
Air
575 nm pump
12.4 keV probe
Crystals
Jungfrau 16M Detector
Interaction point
Period 20 ms
Delay Δt
SwissFEL
LCP catcher
Light
Light
Light
Light
Dark
Light
Light
Light
Light
Dark
...
b.
c.

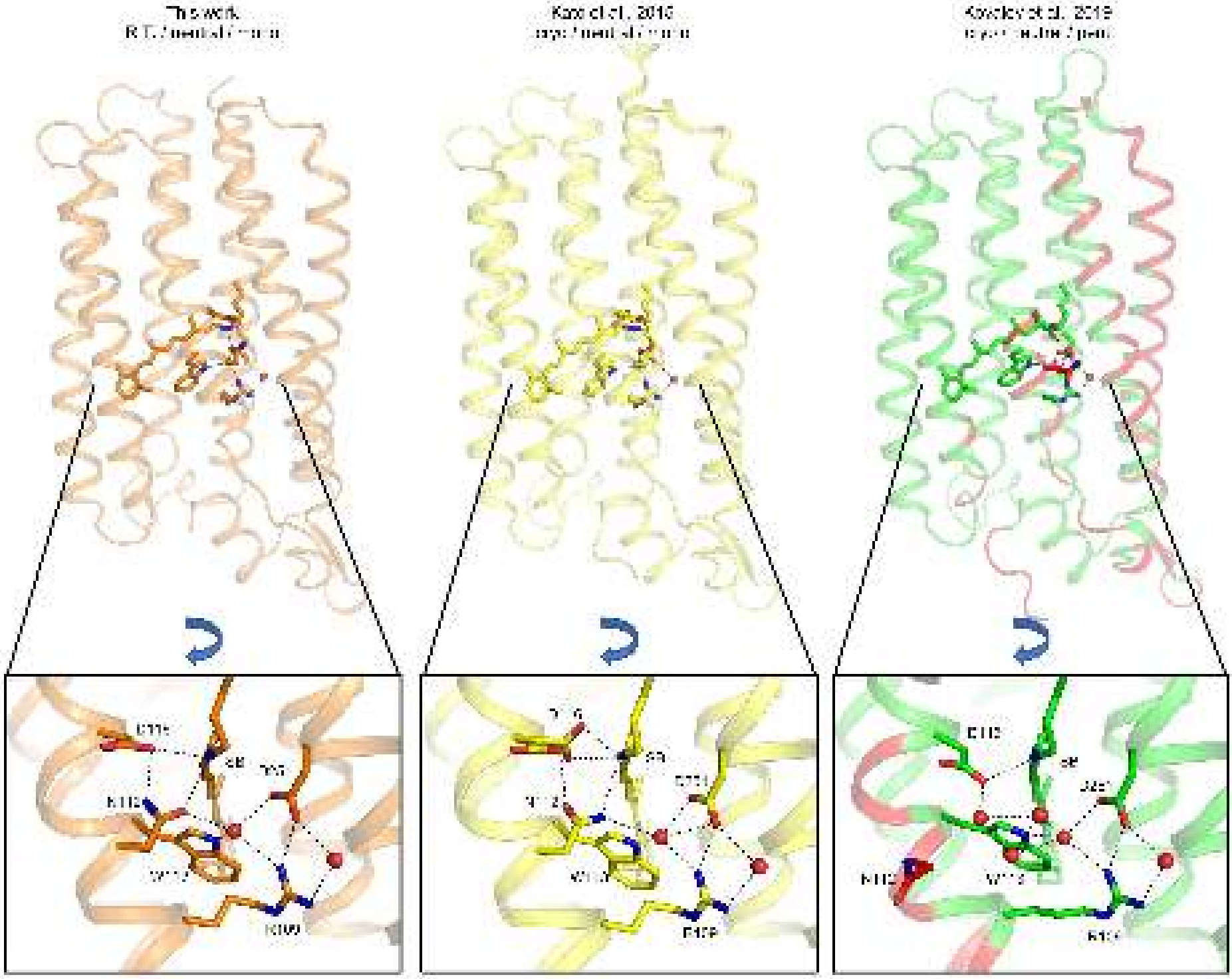
This work
Kato et al. 2016
Kooijman et al. 2019

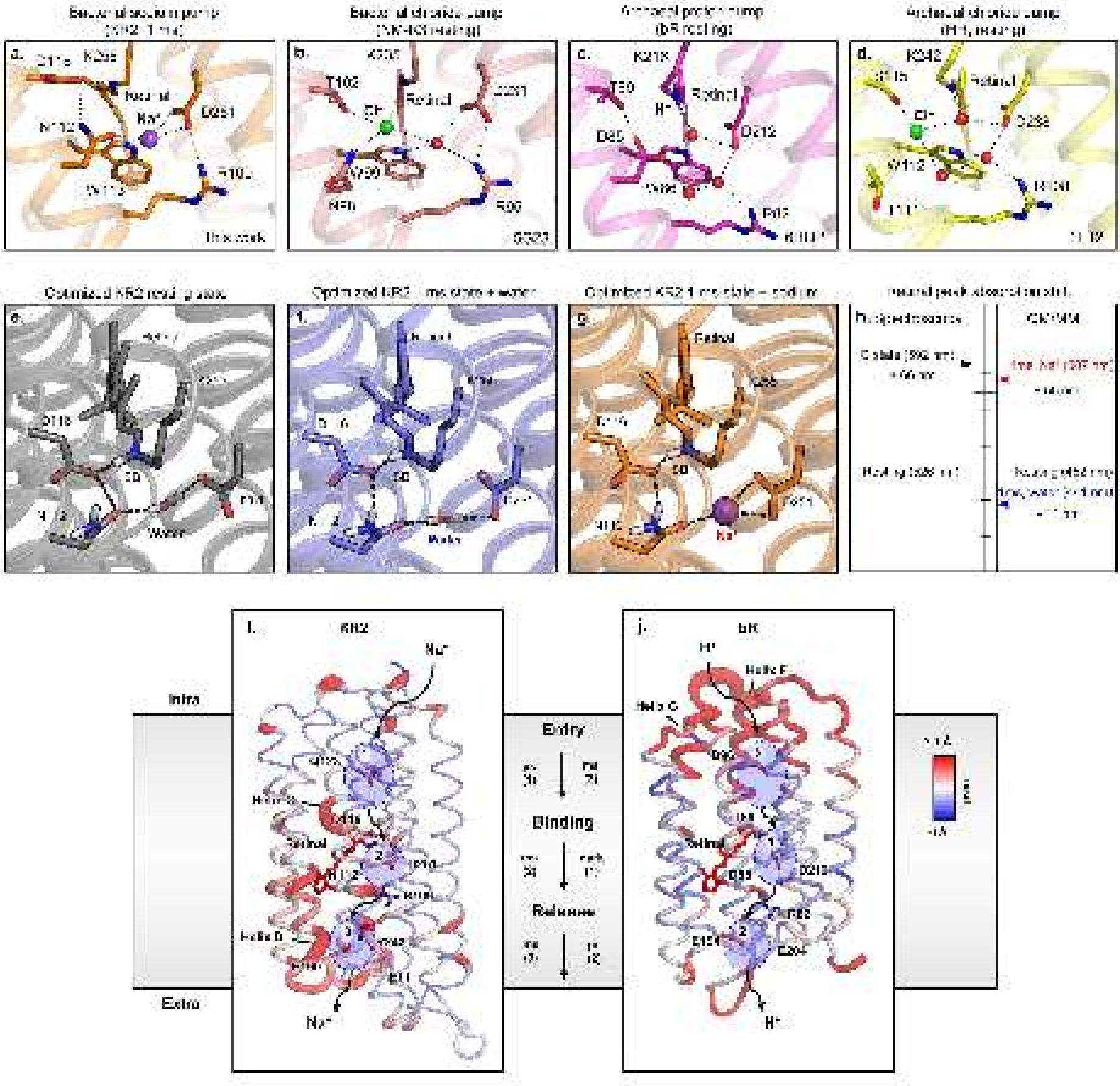
a.
b.
c.
d.
K216
T102
Retinal
D251
D212
D85
Na+
Cl-
H+
Water
e.
f.
g.
h.
Retinal
Water
Na+
i.
KR2
Intra
Extra
Na+
Entry
Binding
Release
j.
bR
H+
Helix F
Helix G
Retinal
D85
D212
D96
D104
D204
H+

	Dark-acidic	Dark-neutral	800 fs	2 ps	100 ps	1 ns	16 ns	1 μs	30 μs	150 μs	1 ms	20 ms	800fs + 2ps	1ns + 16ns	30μs + 150μs
Data collection															
Space group	I222														
Cell dimensions															
a, b, c (Å)	41.5, 84.5, 235.6														
α, β, γ (°)	90, 90, 90														
Indexed patterns	47'518	158'832	47'801	47'595	43'162	45'045	50'165	55'041	50'754	48'383	60'629	48'329	95396	95210	99137
Indexing rate (%)	12.51	11.30	10.68	15.28	9.65	14.11	14.28	11.87	9.00	9.61	12.23	9.16	-	-	-
Overall statistics excluding anisotropic shell 12.4 Å – 2.3 Å (Overall statistics 12.4 Å – 1.60 Å including anisotropic shell)															
Resolution along a*; b*; c* (Å)	2.0; 2.3; 1.6	2.2; 2.3; 1.6	2.1; 2.3; 1.7	2.1; 2.3; 1.7	2.1; 2.20; 1.6	2.1; 2.20; 1.6	2.1; 2.3; 1.7	2.1; 2.3; 1.7	2.1; 2.3; 1.7	2.1; 2.3; 1.7	2.1; 2.2; 1.7	2.1; 2.20; 1.6	2.0; 2.2; 1.6	2.0; 2.2; 1.6	2.0; 2.2; 1.6
No. reflections	18'807 (28'904)	18'873 (31'741)	18'840 (26'799)	18'840 (27'107)	18'872 (29'755)	18'847 (28'057)	18'827 (26'141)	18'828 (26'237)	18'793 (25'531)	18'812 (26'123)	18'847 (27'051)	18'863 (29'034)	18'874 (29'870)	18'872 (30'047)	18'861 (28'402)
Completeness (%)	99.7 (52.3)	100 (57.5)	99.8 (48.5)	99.8 (49.1)	100 (53.9)	99.9 (50.8)	99.8 (47.3)	99.8 (47.5)	99.6 (46.2)	99.7 (47.3)	99.9 (49.0)	99.9 (52.6)	100 (54.1)	100 (54.4)	99.9 (51.4)
Multiplicity	608 (505)	1'640 (1'328)	522 (444)	497 (419)	475 (395)	507 (431)	547 (469)	563 (481)	505 (439)	479 (413)	594 (505)	531 (445)	1018 (834)	1053 (869)	983 (827)
R_{split} (%)	6.1 (6.8)	4.3 (4.9)	8.0 (8.6)	8.3 (9.0)	8.4 (9.1)	7.8 (8.4)	7.3 (7.8)	7.4 (8.0)	7.1 (7.7)	7.8 (8.4)	6.9 (7.5)	7.6 (8.2)	5.7 (6.3)	5.3 (5.9)	5.3 (5.9)
$CC_{1/2}$	1.00 (1.00)	1.00 (1.00)	0.99 (0.99)	0.99 (0.99)	0.99 (0.99)	0.99 (0.99)	0.99 (0.99)	0.99 (0.99)	0.99 (0.99)	0.99 (0.99)	0.99 (0.99)	0.99 (0.99)	1.00 (1.00)	1.00 (1.00)	1.00 (1.00)
$\langle I/\sigma(I)\rangle$	11.4 (8.3)	16.5 (11.1)	9.2 (7.1)	9.1 (7.0)	9.2 (6.7)	9.2 (7.0)	9.6 (7.5)	9.7 (7.6)	9.4 (7.5)	9.3 (7.3)	10.4 (7.9)	9.8 (7.2)	12.8 (9.1)	13.1 (9.2)	13.1 (9.6)
High resolution statistics of the anisotropic shell (2.3 Å - 1.60 Å)															
No. reflections	10'097	12'867	7'959	8'267	10'883	9'210	7'314	7'409	6'738	7'311	8'204	10'171	10'996	11'175	9'541
Completeness (%)	27.7	35.4	21.9	22.7	29.9	25.3	20.1	20.4	18.5	20.1	22.6	28.0	30.2	30.7	26.2
Multiplicity	331	872	261	241	256	274	269	272	256	244	302	285	519	559	518
R_{split} (%)	38.3	30.0	43.8	44.3	38.2	41.0	45.2	44.0	45.8	43.8	42.1	38.2	37.0	35.4	37.1
$CC_{1/2}$	0.90	0.95	0.86	0.84	0.89	0.89	0.84	0.86	0.85	0.86	0.87	0.89	0.91	0.92	0.91
$\langle I/\sigma(I)\rangle$	2.5	3.1	2.2	2.2	2.5	2.4	2.2	2.2	2.2	2.2	2.3	2.5	2.6	2.7	2.6

	Dark-acidic	Dark-neutral	800fs + 2ps	1ns + 16ns	30μs + 150μs	1ms	20ms
Data collection							
Space group				I222			
Cell dimensions							
a, b, c (Å)				41.5, 84.5, 235.6			
α, β, γ (°)				90, 90, 90			
Resolution (Å)	12.36 – 1.6* (2.3 – 1.6)	12.36 – 1.6* (2.3 – 1.6)	12.36 – 2.25 (2.33 – 2.25)	12.35 – 2.25 (2.33 – 2.25)	12.35 – 2.25 (2.33 – 2.25)	12.36 – 2.5 (2.58 – 2.5)	12.36 – 2.5 (2.58 – 2.5)
R_{split}	6.8 (38.3)	4.9 (30.0)	5.8 (24.29)	5.4 (24.1)	5.4 (27.3)	6.6 (17.3)	7.4 (17.1)
$\langle I/\sigma(I)\rangle$	8.3 (2.5)	11.1 (3.1)	12.2 (3.5)	12.5 (3.7)	12.5 (3.3)	12.2 (5.1)	11.3 (5.6)
$CC_{1/2}$	1.00 (1.00)	1.00 (1.00)	0.99 (0.95)	0.99 (0.96)	0.99 (0.96)	0.99 (0.97)	0.99 (0.96)
Completeness (%)	52.3 (27.7)*	57.5 (35.4)*	99.9 (98.6)	99.9 (98.6)	99.7 (97.5)	99.9 (100)	99.9 (100)
Multiplicity	505 (331)	1328 (872)	994 (643)	1028 (660)	960 (616)	647 (443)	579 (400)
Refinement							
Resolution (Å)	12.36 – 1.6 (1.64 – 1.6)	12.43 – 1.6 (1.64 – 1.6)	12.36 – 2.25 (2.35 – 2.25)	12.35 – 2.25 (2.35 – 2.25)	12.35 – 2.25 (2.35 – 2.25)	12.36 – 2.5 (2.66 – 2.5)	12.36 – 2.5 (2.66 – 2.5)
No. reflections	28’895 (123)	31’728 (203)	18’021 (1874)	18’073 (1906)	17’917 (1920)	13’446 (2007)	13’268 (1871)
R_{work} / R_{free}	17.67 / 21.3	18.8 / 21.7	27.2 / 32.8	26.5 / 33.2	26.7 / 33.5	25.8 / 32.4	27.8 / 35.3
No. atoms							
Protein	2139	2105	2103	2111	2099	2099	2099
Ligands	242	242	242	242	242	243	243
Water	99	60	53	50	49	49	47
B-factors							
Protein	31.8	36.1	42.1	40.1	33.7	41.7	52.1
Ligands	61.5	62.1	65.6	65.5	53.2	63.6	69.9
Water	46.9	46.1	41.6	43.6	36.3	43.6	50.1
R.m.s. deviations							
Bond lengths (Å)	0.011	0.006	0.008	0.007	0.007	0.007	0.008
Bond angles (°)	1.063	0.735	0.938	0.928	0.928	0.865	0.921
PDB Code	6TK7	6TK6	6TK5	6TK4	6TK3	6TK2	6TK1

* Data are anisotropic, see extended statistics Table 1 and Materials and Methods